© 2021. Published by The Company of Biologists Ltd | Development (2021) 148, dev198044. doi:10.1242/dev.198044

RESEARCH ARTICLE

Regulation of UNC-40/DCC and UNC-6/Netrin by DAF-16 promotes functional rewiring of the injured axon

Atrayee Basu[1], Sibaram Behera[1], Smriti Bhardwaj[1], Shirshendu Dey[2] and Anindya Ghosh-Roy[1,*]

ABSTRACT

The adult nervous system has a limited capacity to regenerate after accidental damage. Post-injury functional restoration requires proper targeting of the injured axon to its postsynaptic cell. Although the initial response to axonal injury has been studied in great detail, it is rather unclear what controls the re-establishment of a functional connection. Using the posterior lateral microtubule neuron in *Caenorhabditis elegans*, we found that after axotomy, the regrowth from the proximal stump towards the ventral side and accumulation of presynaptic machinery along the ventral nerve cord correlated to the functional recovery. We found that the loss of insulin receptor DAF-2 promoted 'ventral targeting' in a DAF-16-dependent manner. We further showed that coordinated activities of DAF-16 in neuron and muscle promoted 'ventral targeting'. In response to axotomy, expression of the Netrin receptor UNC-40 was upregulated in the injured neuron in a DAF-16-dependent manner. In contrast, the DAF-2-DAF-16 axis contributed to the age-related decline in Netrin expression in muscle. Therefore, our study revealed an important role for insulin signaling in regulating the axon guidance molecules during the functional rewiring process.

KEY WORDS: *Caenorhabditis elegans*, Axon regeneration, PLM neuron, Functional restoration, DAF-16, UNC-40

INTRODUCTION

The adult nervous system is vulnerable to accidental damage and injury. Neuronal injury leads to a wide range of behavioral deficits, such as loss of sensation or fatal paralysis. Regeneration from the injured proximal stump and subsequent growth towards the target tissues can lead to a functional recovery (He and Jin, 2016; Laha et al., 2017). For example, after axotomy, *Caenorhabditis elegans* motor neurons can reach the target muscles, which leads to a recovery in locomotion (Yanik et al., 2004; El Bejjani and Hammarlund, 2012). Similarly, in fish, swimming behavior is restored as the axon regrows after spinal cord injury (Becker et al., 1997; Rasmussen and Sagasti, 2017). Axon regeneration potential in an organism declines with age (Geoffroy et al., 2016; Verdú et al., 1995; Basu et al., 2017) for multiple reasons (Fawcett, 2020). First, the intrinsic capacity of the neurons to regenerate diminishes with age (Verdú et al., 1995), and then the external microenvironment poses challenges to the regeneration of the axon (Brosius Lutz and Barres, 2014). Therefore, functional recovery is limited in adulthood. Manipulation of intrinsic pathways and increasing the neural activity together showed some promising effects in the functional restoration of retinal ganglion cells (Lim et al., 2016; Bei et al., 2016). However, the big question about the limiting factors in functional restoration after the accidental damage of axonal processes is still unanswered.

In adulthood, injured axons face a non-permissive environment for correct navigation of the regenerating growth cone (Fawcett, 2020; Fitch and Silver, 2008; Benowitz and Popovich, 2011). Inhibitory axon guidance cues are upregulated following injury in the central nervous system (Giger et al., 2010; Liu et al., 2008). Although nerve injury can trigger expression of axon guidance ligands Slit, Netrin and their receptors, such as Robo and DCC (Chen et al., 2011, 2020; Wang et al., 2019), it is unclear how they are regulated during regeneration. For functional recovery to occur, a regrowing axon must integrate into a neuronal circuit through the formation of proper synapses. Several lines of evidence suggest that the injured neurons can regenerate a synapse (Vidal-Sanz et al., 1987; Oliphint et al., 2010), although it is unclear whether the synaptic transmission can take place through these synapses. Furthermore, it is challenging to correlate behavioral recovery with the anatomical features of axon regeneration at a single neuron level.

Experiments using model organisms have been useful in deciphering the molecular mechanisms underlying the neuronal response to injury (Richardson and Shen, 2019; He and Jin, 2016). The molecular players essential for the regrowth of injured axons have been identified in the past decade (Mahar and Cavalli, 2018; Fawcett and Verhaagen, 2018; Blanquie and Bradke, 2018; Richardson and Shen, 2019). *C. elegans* has been established as an efficient model for studying the mechanism of axonal regeneration (He and Jin, 2016). Conserved Ca^{2+}/cAMP cascade and the Dual leucine zipper kinase (DLK-1) pathway are essential for regrowth (Ghosh-Roy et al., 2010; Hammarlund et al., 2009; Yan et al., 2009). Many other permissive and inhibitory factors have been identified using motor and sensory neurons (Nix et al., 2014; Chen et al., 2011; Kim et al., 2018). For example, the axon regeneration potential of motor neurons declines with age, and is controlled by insulin/IGF signaling pathway (IIS) (Byrne et al., 2014). A clear understanding of the link between axon regeneration and functional rewiring is still lacking. Axotomy of DA9 motor neurons leads to the formation of synapse-like structures in dendritic locations, and behavioral recovery was abnormal (Ding and Hammarlund, 2018). On the other hand, after axotomy of the posterior lateral microtubule (PLM) neuron, self-fusion between the proximal and distal fragments leads to a rapid functional restoration (Basu et al., 2017; Abay et al., 2017). It is unclear whether the injured axons that cannot fuse to their distal counterparts could reach the correct destination and form a synapse. Also, it is unclear whether these events would lead to functional recovery, and mechanistic details underlying these processes remain elusive.

[1]Department of Cellular and Molecular Neuroscience, National Brain Research Centre, Manesar, Nainwal Mode, Gurgaon, Haryana 122051, India. [2]Fluorescence Microscopy Division, Bruker India Scientific PvT Ltd, International Trade Tower, Nehru Place, New Delhi 110019, India.

*Author for correspondence (anindya@nbrc.ac.in)

A.B., 0000-0001-6056-7138; S.B., 0000-0003-1930-9457; A.G.-R., 0000-0002-3428-4588

Handling Editor: François Guillemot
Received 26 October 2020; Accepted 4 May 2021

Development (2021) 148, dev198044. doi:10.1242/dev.198044

Here, using PLM neuron as a model, we correlated the anatomical features of regrowth with functional recovery at the single neuron level. We found that the injured proximal ends, which could reach the ventral nerve cord (VNC) and form a synapse-like structure, contribute to recovery in the touch sensation. Efficient 'ventral targeting' and functional restoration are dependent on the transcription factor DAF-16, which upregulated the Netrin-receptor UNC-40 in the neurons in response to axotomy. In contrast, IIS contributed to the age-related decline in the expression of Netrin/unc-6 in ventral muscle in a DAF-16-dependent manner. Our work elucidates how axon guidance cues are regulated by insulin signaling towards the functional rewiring of an injured neuron.

RESULTS

'Ventral targeting' of injured PLM axon correlates with the recovery in posterior touch sensation

Among the six touch receptor neurons, two PLMs are responsible for sensing the gentle touch in the posterior part of *C. elegans* (Bounoutas and Chalfie, 2007; Basu et al., 2017; Chalfie et al., 1985). A backward moving worm responds to a posterior touch by moving forward. During this response, the PLM neuron inhibits backward movement through an inhibitory chemical synapse to AVA and generates forward movement through an electrical synapse to PVC (Chalfie et al., 1985; Wicks and Rankin, 1995) (Fig. 1A). Previous studies have demonstrated that an axotomized PLM neuron displays two different patterns of regeneration (Fig. 1A) (Basu et al., 2017; Ghosh-Roy et al., 2010; Neumann et al., 2011). In the first category, the regrowing proximal axon can recognize and fuse with its distal part, known as 'fusion'. This self-fusion phenomenon correlates with the rapid restoration of lost touch sensation following axotomy (Basu et al., 2017; Abay et al., 2017) (Fig. 1B). In the second category, the proximal end regrows without fusing with the distal part, named 'non-fusion' events. In this case, the distal end often undergoes degeneration (Ghosh-Roy et al., 2010; Neumann et al., 2011), and functional recovery was not seen at 24 h post-axotomy (Basu et al., 2017) (Fig. 1B). We investigated whether this 'non-fusion' class of regrowth events would eventually lead to a functional recovery at later time points. We found that the posterior touch response index (PTRI) at 48 h post-axotomy was significantly raised to a value of 0.63±0.23 (mean±s.d.) from 0.48±0.16, obtained at 24 h post-axotomy (Fig. 1B; ***P<0.001, Tukey's multiple comparison test). We noticed that some of the events in the whole cohort of the 'non-fusion' category showed PTRI values comparable with that of the 'fusion' category (Fig. 1B). We speculated that these events might represent the regrowth events with correct targeting. We noticed that the proximal part often regrew towards the ventral cord by making a branch (arrowhead, Fig. 1Ca) or turning towards the ventral side (arrowhead, Fig. 1Cb). We classified these events as 'ventral targeting' (Fig. 1C). In other 'non-fusion' events, the proximal axon regrew either towards the dorsal side (Fig. 1Cc) or towards the anterior direction (Fig. 1A), or sprouted multiple small branches (Fig. 1Cd). To compare the functional recovery across various regrowth patterns, we used the 'recovery index' (RI) as the ratio of the 'PTRI at 24 h or 48 h post-axotomy' to the 'PTRI just after axotomy'. Any RI value above 1 (green dotted line, Fig. 1D) indicates a sign of recovery. We noticed that the RIs of 'ventral targeting' events at 24 h and 48 h were 1.69±0.78 and 2.22±1.09 (mean±s.d.), respectively (Fig. 1D), whereas the RIs corresponding to all the other categories were below 1 (Fig. 1D), indicating no functional restoration. Overall, the RI of the 'non-ventral' events was significantly lower than the 'ventral targeting' events (Fig. S1A). The recovery values corresponding to the 'ventral' category were comparable with that of the 'fusion' class at 48 h post-axotomy (Fig. 1D). Moreover, we saw that the percentage of 'ventral targeting' events increased from 27% at 24 h to 45% at 48 h post-axotomy (**P<0.01, Fisher's exact test). This possibly explains the overall increase in the PTRI values at 48 h in the 'non-fusion' events (Fig. 1B).

The PLM neuron has a ventral branch (arrowhead, Fig. 1A), which makes en passant synapse to AVA interneuron at the VNC (Schaefer et al., 2000; White et al., 1986). We speculated that the 'ventral targeting' might lead to an enrichment of the presynaptic proteins at the tip of the regrowing axon. Therefore, we analyzed the localization of presynaptic reporter GFP::RAB-3 (Luo et al., 2014) in different regrowth events. In the case of 'ventral targeting' events, we saw an accumulation of GFP::RAB-3 at the VNC (white arrowheads, Fig. 1E). This accumulation pattern resembled the RAB-3 punctae seen at the end of the synaptic branch of PLM neuron (arrowheads, Fig. 1F), which we termed as 'developmental synapse'. In the case of a developmental synapse, before axotomy, the ratio of GFP::RAB-3 versus a cytosolic marker mScarlet was 1.70±0.61 (mean±s.d.) at the region of interest (ROI) placed near the synapse (rectangular ROI, Fig. 1F,G). This value was comparable with the ratio obtained for the 'ventral targeting' events during regeneration (Fig. 1E,G). The normalized value of GFP::RAB-3 at the tip of the regrowing axon in the 'non-ventral' class (Fig. S1B) was significantly lower than the 'ventral targeting' events (Fig. 1G). The RI corresponding to the 'ventral targeting' events with the RAB-3 enrichment in the transgenic background expressing GFP::RAB-3 was 1.83±0.84, which was significantly higher than the value obtained in the case of 'non-ventral' events (Fig. S1C). This phenomenon was similar to what has been seen in *muIs32* [P*mec-7*-GFP] transgenic background (Fig. 1D). This suggested that the functional recovery related to 'ventral targeting' of the injured PLM axon is not the artefact of the transgenic reporter. Another presynaptic reporter, ELKS-1::TagRFP (Zheng et al., 2014), also showed an enrichment at the VNC in the case of 'ventral targeting' events (arrowheads, Fig. S1D). Similarly, the postsynaptic receptor GLR-1::GFP (Hoerndli et al., 2015) aligned along the ventral cord in the 'ventrally targeted' axon (arrowheads, Fig. S1E). This helped us to conclude that the regrowth towards the ventral side and enrichment of presynaptic machinery at the ventral cord leads to the functional recovery during axon regeneration.

'Ventral targeting' and functional restoration are compromised in adulthood

Axon regeneration potential in adulthood is limited (Verdú et al., 1995; Kang and Lichtman, 2013; Graciarena et al., 2014). A previous study in touch neurons showed that functional restoration through axonal self-fusion decreases with age (Basu et al., 2017). Therefore, we investigated whether the accuracy in axon guidance during regrowth would decrease in adulthood. We found that the RI corresponding to the 'non-fusion' events gradually decreased with age (Fig. 2A). The RI at A3 stage became 0.91±0.57 (mean±s.d.), which is significantly lower than the value obtained at L4 stage (***P<0.001, Tukey's multiple comparison test) (Fig. 2A). Investigation of the regrowth pattern revealed that the percentage of 'ventral targeting' events was significantly decreased when axotomy was carried out at the A3 stage (Fig. 2B), although the total regrowth was unperturbed (Fig. 2C). Moreover, the total regrowth length in the 'non-ventral' and 'ventral' class was comparable (Fig. 2C). Another phenomenon we noticed was that the RI corresponding to the 'ventral targeting' events at the A3 stage was significantly decreased compared with the L4 stage (**P<0.01, Tukey's multiple comparison test; Fig. 2D). This suggested that 'ventral targeting' is not enough for functional recovery in an older animal.

Development (2021) 148, dev198044. doi:10.1242/dev.198044

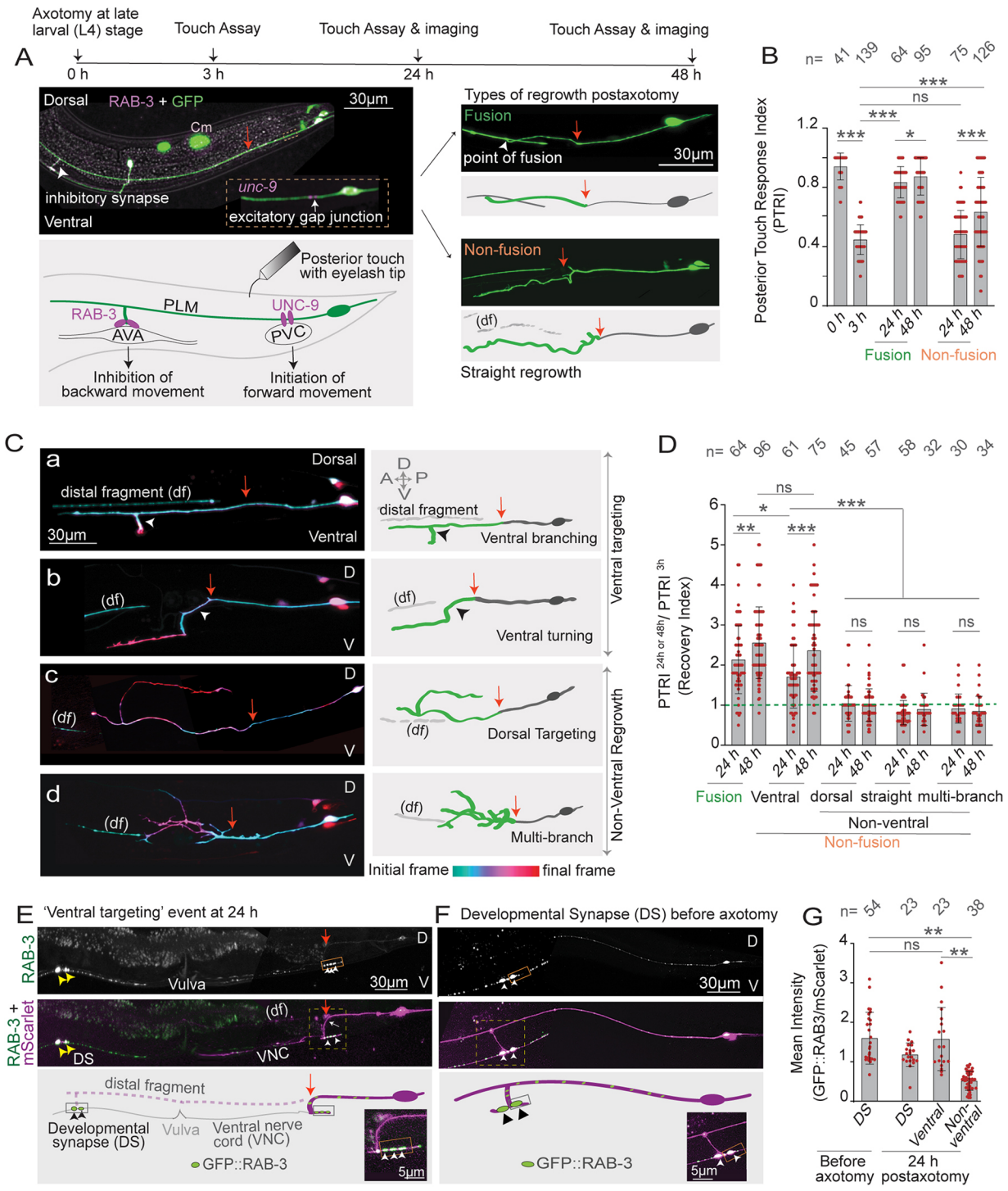

Fig. 1. 'Ventral targeting' events during regeneration of PLM axon correlate with functional restoration. (A) The experimental set-up for the axotomy of PLM neuron [labeled with P*mec-7*::GFP (*muIs32*) and P*mec-4*::mCherry::RAB-3 (*tbIs227*)] at the L4 stage, and follow-up steps to correlate functional recovery with regrowth patterns. The PTRI was measured at 3 h post-axotomy to measure the functional drop after injury. Similarly, the PTRI was measured at 24 h or 48 h post-axotomy to evaluate the extent of functional recovery, following which the axon regrowth pattern in the same animal was imaged. The confocal images of two major regrowth patterns are shown. The red arrow indicates the site of injury. The worm illustration describes how PLM neuron is connected to the AVA and PVC interneurons. UNC-9::GFP [*shrEx435*] was used to label the electrical synapse. 'Cm' represents the co-injection GFP-reporter in coelomocyte. (B) The PTRI values corresponding to the 'fusion' and 'non-fusion' events at 24 h and 48 h post-axotomy at L4 stage. *N* (independent replicates)=4-12. (C) The depth-coded pseudocolored *z*-stacked confocal images and illustrations of various regrowth patterns. The arrowheads indicate the regrowth towards the ventral direction and red arrows indicate the injury site. (D) The quantification of the RI expressed as PTRI at 24 h post-axotomy/PTRI at 3 h post-axotomy for different regrowth trajectories. The dashed green line denotes an RI value of 1. *N*=6-8. (E,F) Confocal images of PLM expressing P*mec-7*::GFP::RAB-3 (*jsIs821*) and P*mec-4*::mScarlet (*shrEx209*). (E) The large puncta of GFP::RAB-3 can be observed at the tip of the ventrally targeted axon along the VNC. (F) The enrichment of GFP::RAB-3 (arrowheads) at the end of the synaptic branch also referred to as developmental synapse (DS). Insets show an enlarged view of the region inside the yellow dashed box. (G) The ratio of GFP::RAB-3 intensity to the intensity of mScarlet from the rectangular ROIs shown in E and F. *N*=3-5. Red arrows indicate the site of injury. The yellow and white arrowheads represent the GFP::RAB-3 enrichment along the VNC in the case of the ventrally targeted axon and the developmental synapse, respectively. Data are mean±s.d. **P*<0.05; ***P*<0.01; ****P*<0.001; ns, non-significant (ANOVA with Tukey's multiple comparisons test).

Development (2021) 148, dev198044. doi:10.1242/dev.198044

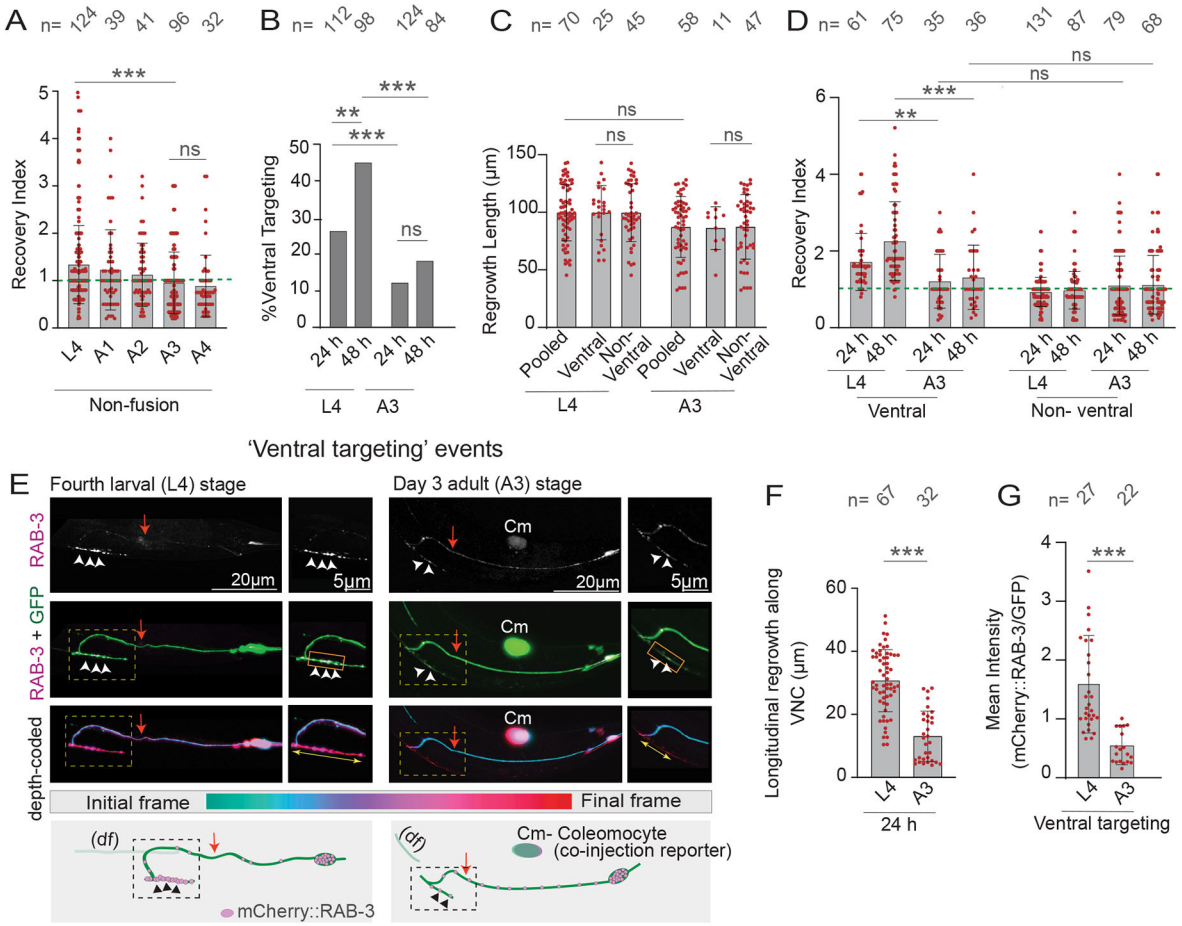

Fig. 2. Age-related decline in 'ventral targeting' and functional restoration. (A) RI values corresponding to the 'non-fusion' events at 24 h post-axotomy performed at different stages of adulthood. *N* (independent replicates)=3-8. (B) The percentage of 'ventral targeting' events at L4 and A3 stages. *N*=3-9. (C) Regrowth length corresponding to the 'cumulated non-fusion' events termed as 'pooled,' 'ventral' and 'non-ventral' events at 24 h post-axotomy. *N*=4-5. (D) RI values corresponding to the 'ventral' and 'non-ventral' regrowth events at L4 and A3 stages. *N*=6-9. (E) Examples of 'ventral targeting' events after axotomy at L4 and A3 stages. The worms are expressing P*mec-4*::mCherry::RAB-3 [*tbIs227*] and P*mec-7*::GFP [*muIs32*] reporters. The arrowheads indicate the RAB-3 enrichment along the VNC. 'Cm' represents the co-injection GFP-reporter in coelomocyte. The depth-coded images of the GFP channel were separately presented to highlight the regrowth along the VNC (double-headed yellow arrows). Insets show an enlarged view of the region inside the yellow dashed box. The red arrow indicates the site of injury. (F) Comparison of the longitudinal regrowth along the VNC (double-headed yellow arrows) at 24 h post-axotomy. *N*=3-4. (G) The ratio of mCherry::RAB-3 intensity normalized to the GFP intensity from the ROIs at the tip of the regenerated axon as shown in E. *N*=5. Data are mean±s.d. ***P*<0.01; ****P*<0.001; ns, non-significant [ANOVA with Tukey's multiple comparisons test (A,C,D); Fisher's exact test (B); Mann–Whitney unpaired non-parametric two-tailed Student's *t*-test (F,G)].

We saw that at the A3 stage, in case the regrowing axons reached the VNC, the longitudinal growth along the cord (double-headed yellow arrows, Fig. 2E) was less compared with that at the L4 stage (Fig. 2F). Moreover, the ratio of mCherry::RAB-3 (Sood et al., 2018) versus GFP in the rectangular ROI placed at the VNC (Fig. 2E) was significantly decreased at the A3 stage (****P*<0.001, Tukey's multiple comparison test; Fig. 2G). In the background expressing mCherry::RAB-3 reporter, the percentage of 'ventral targeting' and the RI corresponding to the 'ventral targeting' event significantly decreased at the A3 stage (Fig. S2A,B). This observation strengthens the conclusion that the age-related decrease in ventral guidance during axon regeneration is not an artefact of transgenic background.

Insulin receptor DAF-2 and downstream transcription factor DAF-16 control ventral guidance of the regenerating axon

Efforts in the past decade helped to identify the pathways regulating the axon regeneration potential in the worm (Nix et al., 2014; Chen et al., 2011; Kim et al., 2018). However, how axon regeneration pathways control functional rewiring has not yet been addressed. Removal of the cell-intrinsic inhibitory pathways enhances the regenerative outgrowth following axotomy (He and Jin, 2016). We investigated whether the mutants with enhanced axon regrowth ability (Chen et al., 2011; Nix et al., 2014; Knowlton et al., 2017; Zou et al., 2013; Kosmaczewski et al., 2015; Hubert et al., 2014; Alam et al., 2016; Table S1) would have better functional recovery. We also tested the mutants with enhanced lifespan (Murphy and Hu, 2013; Byrne et al., 2014; Taub et al., 2018; Senchuk et al., 2018) and healthspan (Bansal et al., 2015; Yuan et al., 2012; Table S1), as their role in touch neuron regeneration is not clear yet. We compared the recovery indices of 'non-fusion' events at L4 and A3 stages to find the possible regulators for axon regeneration in adulthood. Although some of the mutants showed an enhanced functional restoration in the L4 stage (Fig. S3A), the recovery indices in those mutants at A3 stage were not significantly different from the value obtained in the wild-type control (Fig. S3B). There were a few exceptions, such as *akt-1(lf)*, *sgk-1(lf)*, *rsks-1(lf)* and *let-7(lf)*, which showed an RI above 2. This was significantly higher than the RI in wild type at L4 and A3 (Fig. S3A,B).

Development (2021) 148, dev198044. doi:10.1242/dev.198044

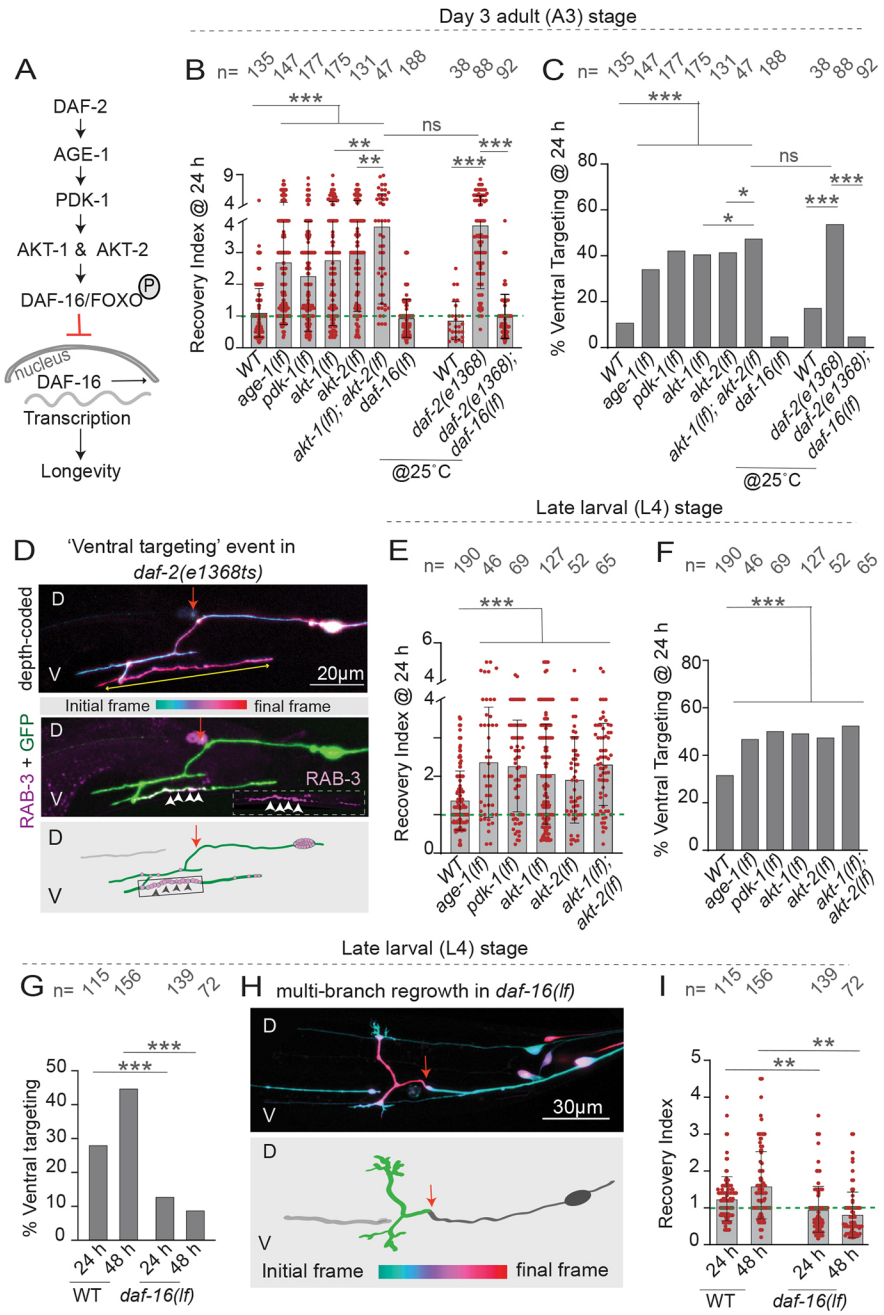

Fig. 3. Downregulation of insulin receptor enhances 'ventral targeting' and functional restoration in a *daf-16*-dependent manner. (A) Pathway diagram showing how insulin signaling regulates lifespan. (B,C) RI values (B) and percentage of 'ventral targeting' (C) corresponding to the 'non-fusion' regrowth events in the mutants affecting either DAF-2 or downstream kinases at 24 h post-axotomy performed at the A3 stage. Similar analysis was also performed in *daf-16(lf)* and *daf-2(e1368ts); daf-16(lf)*. For B and C, *N* (independent replicates)=3-9. (D) An example of a 'ventral targeting' event in *daf-2(e1386ts)* at A3 stage. The neuron is co-expressing P*mec-4*::mCherry::RAB-3 (*tbIs227*) and P*mec-7*::GFP (*muIs32*). The depth-coded image of the GFP channel was presented separately to show the regrowth along the VNC (double-headed yellow arrow). The arrowheads indicate mCherry::RAB-3 enrichment along the VNC. (E,F) The RI values (E) and the percentage of 'ventral targeting' events (F) in the mutants affecting IIS at 24 h post-axotomy performed at the L4 stage. For E and F, *N*=3-6. (G) The percentage 'ventral targeting' events in wild type (WT) and *daf-16(lf)* after axotomy performed at the L4 stage. *N*=5-8. (H) Depth-coded confocal image of the multibranch regrowth pattern in *daf-16(lf)*. (I) RI values in wild type and *daf-16(lf)* at 24 h and 48 h post-axotomy performed at the L4 stage. *N*=5-8. Broken *y*-axes were used in the plots in B and E. Red arrows indicate the site of injury, and arrowheads indicate the mCherry::RAB-3 punctae. Data are mean±s.d. **P*<0.05; ***P*<0.01; ****P*<0.001; ns, not significant [ANOVA with Tukey's multiple comparisons test (B,E,I); Fisher's exact test (C,F,G)].

The AKT-1 kinase acts downstream to the insulin receptor DAF-2 (Fig. 3A) to regulate the lifespan of *C. elegans* (Murphy and Hu, 2013). It was observed that the insulin signaling downregulates the axon regrowth capacity of D-type motor neuron in older animals (Byrne et al., 2014). Therefore, we tested *daf-2 (e1368ts)* and the mutants that inactivate downstream kinases in IIS, such as *age-1*, *pdk-1*, *akt-1* and *akt-2*. All of these mutants showed significantly enhanced functional recovery (****P*<0.001, Tukey's multiple comparison test) compared with the wild-type control at A3 stage (Fig. 3B). Reduced IIS promotes longevity through the upregulation of the transcriptional activity of DAF-16 (Libina et al., 2003; Murphy and Hu, 2013) (Fig. 3A). Consistently, we found that the enhanced RI seen in the *daf-2* mutant was completely dependent on *daf-16* (Fig. 3B). We examined whether the enhanced functional recovery due to loss of IIS correlates with the enhanced 'ventral targeting'. The mutants for IIS displayed a higher percentage of 'ventral targeting' events than wild type (Fig. 3C). Additionally, the recovery indices corresponding to the 'ventral targeting' events were significantly higher in these mutants (Fig. S3C). In *daf-2* mutant, the longitudinal growth along the VNC was 53.50±14.27 µm (mean±s.d.) compared with 14.0±8.34 µm in wild type (****P*<0.001, Mann–Whitney comparison *t*-test). More RAB-3 punctae were accumulated along the VNC in *daf-2(lf)* (arrowheads, Fig. 3D). A similar observation was also made in the mutants of IIS at L4 stage. For example, both the RI and the percentage of 'ventral targeting' events were significantly enhanced in these mutants, even at L4 stage (Fig. 3E,F). Therefore, IIS controls the guidance of the regrowing PLM axon irrespective of age. The percentage of 'ventral targeting' was significantly reduced in the *daf-16* single mutant background at L4 stage (****P*<0.001, Fisher's exact test; Fig. 3G), although total regrowth was not reduced (Fig. S3D). Often, in *daf-16(lf)*, we noticed a multibranch

Development (2021) 148, dev198044. doi:10.1242/dev.198044

regrowth pattern (Fig. 3H) that did not sufficiently grow towards the VNC. Consistent with these data, the RI in *daf-16(lf)* at the L4 stage was significantly less than the wild type (Fig. 3I). Therefore, our observation indicated that FOXO family transcription factor DAF-16 is required for ventral guidance and functional restoration independent of insulin signaling.

DAF-16 is required both in neuron and muscle for ventral guidance of injured proximal axon

As DAF-16 is expressed in multiple tissues, including neurons, it was important to test the tissue-specific requirement of this protein in the axon regrowth of PLM neuron. As *daf-16(mu86)* affects both the 'a' and 'f' isoform of *daf-16* (Chen et al., 2015), we expressed both isoforms for the rescue experiments. We expressed them in *daf-16*-expressing cells, intestine, neurons, muscle and epidermis in the *daf-16* mutant background. The recovery indices due to pan-neuronal and touch neuron-specific expression of *daf-16f* in *daf-16(lf)* were 1.50±1.14 and 1.74±1.34 (mean±s.d.), respectively. These values were significantly higher (***P<0.001, Tukey's multiple comparison test) than the *daf-16* mutant (Fig. 4A). The drop in the percentage of 'ventral targeting' was also rescued by the neuron-specific expression of *daf-16f* (Fig. 4B). Similarly, the neuron-specific expression of *daf-2* significantly rescued the enhanced functional restoration and 'ventral targeting' events seen in *daf-2(m596)* (Fig. S4A,B). This was consistent with the previous report on motor neuron regeneration (Byrne et al., 2014). However, surprisingly, the muscle-specific expression of *daf-16f* could also rescue the phenotype in *daf-16(lf)* to a similar extent (Fig. 4A,B). Simultaneous expression of the f isoform in touch neuron and muscle resulted in a synergistic increase in the RI and 'ventral targeting', which was akin to the rescue of *daf-16(lf)* using its own promoter (Fig. 4A,B). The lack of longitudinal regrowth along the ventral cord in *daf-16(lf)* was rescued by both neuron and muscle-specific expression of *daf-16f* (Fig. 4C,D). Expression of *daf-16f* in the intestine or in the epidermis did not result in any improvement in the phenotype in the *daf-16* mutant (Fig. 4A,B). Neuron-specific expression of the *daf-16a* isoform also rescued the 'ventral targeting' and RI value in *daf-16(lf)* (Fig. S4C,D). However, when *daf-16a* isoform was driven in muscle it showed a milder rescue, indicating that the N-terminal region of the f isoform was needed for the optimal function in muscle cells. Tissue-specific rescue experiments suggested that the functional rewiring process is independent of IGF-1/IIS activity in the intestine. However, the function of IIS in axon regeneration is not solely neuron intrinsic as found in motor neurons (Byrne et al., 2014). Neuron-intrinsic activity of DAF-16 is facilitated by its muscle-specific activity in the PLM neuron.

Age-dependent decline in the regeneration of D-type motor neuron was correlated to the drop in the expression of *dlk-1*, which is also a transcriptional target of DAF-16 (Byrne et al., 2014). We saw that DLK-1 is essential for axon regeneration and functional recovery both in wild-type and *daf-2(lf)* backgrounds (Fig. S4E,F). DLK-1 is sufficient to promote axon regrowth after neuronal injury (Yan et al., 2009; Hammarlund et al., 2009). However, the role of DLK-1 MAP kinase in the guidance of regrowing axons is unclear. We tested whether DLK-1 is also sufficient to promote 'ventral targeting' and functional restoration. Upon overexpression of DLK-1 in neuron, axon regrowth was significantly enhanced in both wild-type and *daf-16(lf)* backgrounds (Fig. 4E,F). However, neither 'ventral targeting' nor functional restoration were enhanced in the same backgrounds (Fig. 4G,H). Upon the overexpression of DLK-1, the injured axons regrew straight in the anterior direction (arrowheads, Fig. 4E). Therefore, the percentage of 'ventral targeting' events was significantly reduced upon DLK-1 overexpression in the wild-type background (Fig. 4G). This correlated with the reduced value of the RI due to overexpression of DLK-1 (Fig. 4H). This indicated that the 'ventral targeting' phenomenon related to the function of DAF-16 probably does not involve its target DLK-1.

DAF-16 promotes the expression of UNC-40 in injured PLM neuron

DAF-16 regulates many biological processes in adulthood, including longevity by promoting the expression of its transcriptional targets (Murphy, 2006; Kaletsky et al., 2016). The neuronal targets of DAF-16 have been identified by sequencing the mRNAs isolated from neurons in the *daf-16* mutant (Kaletsky et al., 2016). The authors found ∼9000 neuronal genes differentially regulated by DAF-16. We performed a gene ontology (GO) analysis on these 9000 genes using the specific GO term (GO:0097485) involving 'neuronal projection and guidance', which revealed 110 genes (Table S4). Among these, *unc-40* and *unc-6*, are related to axon guidance. The receptor for the chemoattractant 'netrin'/UNC-6, also known as 'Deleted in colorectal cancer' (DCC)/UNC-40, regulates ventral guidance of growth cone during axon development (Chisholm et al., 2016; Kennedy et al., 1994; Ishii et al., 1992; Chan et al., 1996). The *unc-6/unc-40/slt-1* pathway antagonizes the Wnt planar polarity signaling to establish the ventral branch in PLM neuron (Chen et al., 2017). The promoter of the *unc-40* gene has the binding site 'TGTTTA' for DAF-16 (Fig. 5A), which was also experimentally verified (Gerstein et al., 2010; Celniker et al., 2009). After axotomy, we found that the 'ventral targeting' events were drastically reduced in both *unc-6* and *unc-40* mutants (Fig. 5B); however, axon regrowth was not reduced (Fig. S5A). As these mutants show a partially penetrant phenotype of having no branch (Fig. S5B,C), we used the PLMs with a branch for our axotomy experiments. Similarly, the RI was also reduced in these mutants (Fig. 5C). Enhanced 'ventral targeting' and RI seen due to the overexpression of *daf-16f* in the neuron were significantly reduced in the absence of *unc-40* or *unc-6* in the transgenic background (Fig. 5B,C). Similarly, the loss of *unc-6* reduced the enhanced 'ventral targeting' and RI obtained due to the overexpression of *daf-16f* in the muscle (Fig. 5B,C). A similar result was also obtained in *akt-1(lf)* background (Fig. 5B,C), which upregulates DAF-16 activity (Paradis and Ruvkun, 1998).

We speculated that ventral guidance might be compromised in the *daf-16(lf)* due to a reduced expression of *unc-40*. Additionally, in response to axotomy, *unc-40* could be upregulated in PLM neuron in a *daf-16*-dependent manner. We looked at the transcriptional cum translational reporter of UNC-40, P*unc-40*::UNC-40::GFP (Chan et al., 1996), in wild type and *daf-16(lf)*. We compared the intensity of UNC-40::GFP in the cell body of PLM neuron before and after axotomy, with respect to a diffusible marker mScarlet (Yellow dashed ROIs, Fig. 5D). The normalized intensity of UNC-40::GFP before axotomy was significantly increased in the *daf-2(e1368ts)* background compared to the wild-type control in a *daf-16*-dependent manner (Fig. 5D,F). However, the mean intensity of mScarlet was unaffected in the mutant (Fig. S5E). This ratio was significantly lower in *daf-16(lf)* than wild type before axotomy (Fig. 5D,F). After axotomy, the intensity of UNC-40::GFP in the cell body showed a steady increase with time (Fig. 5D,F; Fig. S5D). Similarly, the UNC-40::GFP intensity gradually increased at the tip of the cut axon following axotomy (rectangular ROIs, Fig. 5E,G; Fig. S5F). However, this axotomy-driven steady increase in UNC-40::GFP, both in the cell body and the axon tip, was significantly

Development (2021) 148, dev198044. doi:10.1242/dev.198044

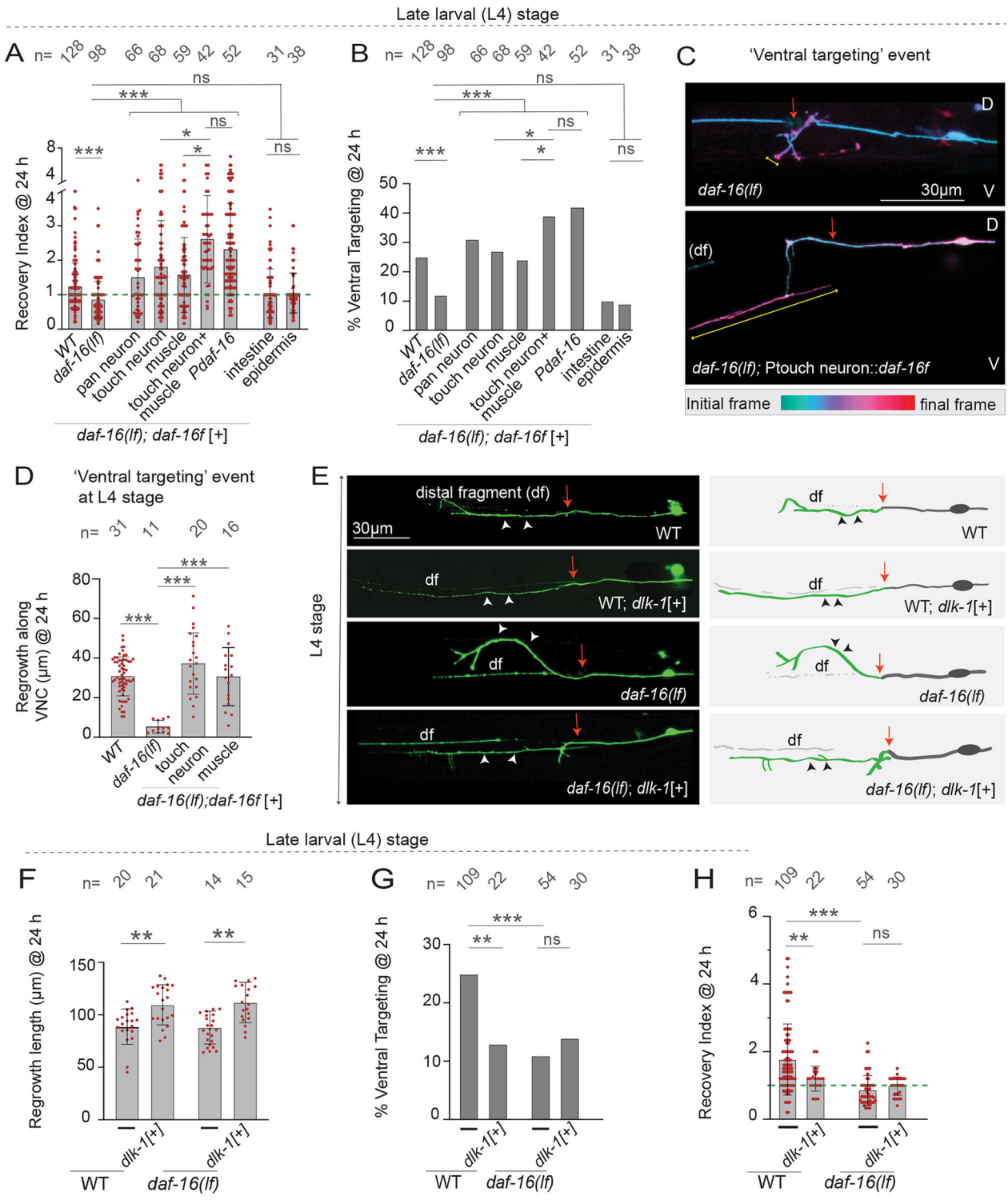

Fig. 4. Synergistic effect of the neuron and muscle-specific expression of *daf-16* in 'ventral targeting' and functional recovery. (A,B) RI values (A) and percentage of 'ventral targeting' events (B) in *daf-16(lf)* with or without the *daf-16f* transgene expressed under the endogenous promoter P*daf-16* [*muEx248*], intestinal promoter P*ges-1* [*muIs142*], pan neuronal promoter P*rgef-1* [*shrEx318*], touch neuron-promoter P*mec-4* [*shrEx226*], muscle-promoter P*myo-3* [*shrEx314*] and epidermal promoter P*dpy-7* [*shrEx316*]. The transgene *shrEx320* was used to co-express *daf-16f* in touch neuron and muscle. A two-segmented *y*-axis was used in plot A. For A and B, *N* (independent replicates)=3-9. (C) The depth-coded images of 'ventral targeting' events at 24 h post-axotomy performed in *daf-16(lf)* and *daf-16(lf)*;P*mec-4*::*daf-16f* [*shrEx226*] background at L4 stage. The double-headed arrow represents regrowth along the VNC. (D) The longitudinal regrowth along the VNC at 24 h post-axotomy performed with L4 worms in wild type (WT) and *daf-16(lf)* with or without rescue transgenes. *shrEx226* and *shrEx314* was used to drive *daf-16f* in touch neuron and muscle, respectively. *N*=3-5. (E) Confocal images and illustrations of the regrowth patterns seen due to the expression of P*mec-4*::*dlk-1[+]* in the wild-type [*shrEx389*] and *daf-16(lf)* [*shrEx391*] backgrounds at 24 h post-axotomy. The arrowheads represent regrowth from the proximal stump. The red arrow indicates the site of injury. (F,H) Regrowth length (F), percentage of 'ventral targeting' (G) and RI values (H) at 24 h post-axotomy in wild-type and *daf-16(lf)* backgrounds, as shown in E. *N*=2-4. Data are mean±s.d. **P*<0.05; ***P*<0.01; ****P*<0.001; ns, non-significant [ANOVA with Tukey's multiple comparisons test (A,D,F,H); Fisher's exact test (B,G)]. Data are mean±s.d.

Development (2021) 148, dev198044. doi:10.1242/dev.198044

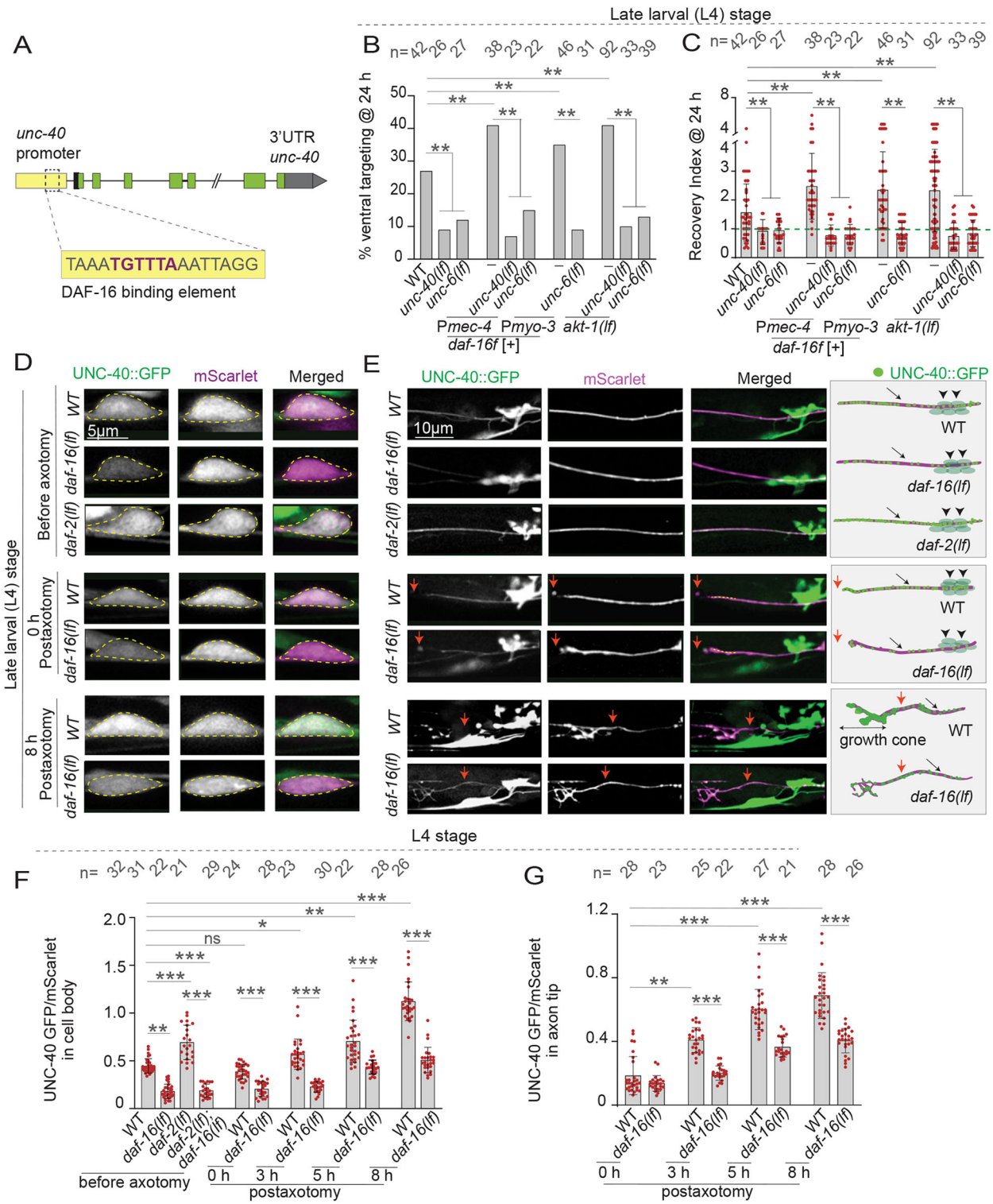

Fig. 5. The expression of the Netrin receptor UNC-40 is downregulated in daf-16 mutant. (A) The DAF-16 binding sequence in the promoter (yellow box) of the *unc-40* gene is highlighted. (B,C) The percentage of 'ventral targeting' events (B) and the RI values (C) at 24 h post-axotomy in the *unc-40(lf)* and *unc-6(lf)* backgrounds with or without the *daf-16f* transgenes expressed under touch neuron-specific promoter P*mec-4* [*shrEx436*] or muscle-specific promoter P*myo-3* [*shrEx437*]. Similar data were also shown in *akt-1(lf)* background with or without the mutations in *unc-6* or *unc-40* genes. *N* (independent replicates)=2-6. (D,E) The confocal images of PLM cell body (D) and PLM axon (E) co-expressing the P*unc-40*::UNC-40::GFP [*icIs132*] and P*mec-4*::mScarlet [*shrEx209*] in wild type (WT) and *daf-16(lf)* before and after axotomy. For cell body, a single *z*-plane is shown (D). Two to four *z*-planes were projected to show the tip of the regrowing axon (E). The observations for E are illustrated on the right side. The yellow dotted ROIs on the cell body and axon were used to measure the intensity of UNC-40::GFP and mScarlet before and after axotomy. The red arrows represent the site of injury. The black arrows and arrowheads represent the PLM axon and other UNC-40::GFP-expressing cells, respectively. (F) The mean intensity of UNC-40::GFP normalized to mScarlet from the ROI on the cell body. *N*=3-8. (G) The mean intensities of UNC-40::GFP normalized to mScarlet from the ROI on axon. *N*=3-8. Data are mean±s.d. **P*<0.05; ***P*<0.01; ****P*<0.001; ns, non-significant [Fisher's exact test (B); ANOVA with Tukey's multiple comparisons test (C,F,G)].

Development (2021) 148, dev198044. doi:10.1242/dev.198044

perturbed in the *daf-16(lf)* background (Fig. 5D-G; Fig. S5D-G). Therefore, as the *unc-40* level is low, the regrowing axons in the *daf-16* mutant may not be sufficiently attracted towards the ventral side in response to 'Netrin' cues.

The expression of UNC-6 in ventral muscle is dependent on the DAF-2-DAF-16 axis

To understand the muscle-specific role of DAF-16 in the ventral guidance of regenerating axons, we speculated that DAF-16 could regulate the guidance cues that are secreted by the muscle. This was also reflected in the transcriptomics data, which suggested that the level of *unc-6* was increased due to loss of *daf-2* in a *daf-16*-dependent manner (Kaletsky et al., 2016; Table S4). UNC-6 is expressed and secreted from the ventral muscles (Ishii et al., 1992; Weinberg et al., 2018). We investigated how *unc-6* expression is regulated in adulthood using a fosmid reporter of *unc-6* (*unc-6::SL2::NLS::YFP::H2B*), which has been shown to express in ventral muscles (Asakura et al., 2010; Weinberg et al., 2018). The nuclei of the 16 ventral muscles along the VNC showed the localization of this reporter (white arrowheads, Fig. 6A) (Asakura et al., 2010). We named the four pairs of nuclei from tail to vulva as 'posterior nuclei', and the rest of the four pairs from the vulva to pharynx as 'anterior nuclei' (arrowheads, Fig. 6A). The expression of this reporter was considerably reduced at the A3 stage (arrowheads, Fig. 6B) to negligible levels. Consequently, the number of visible nuclei significantly dropped at the A3 stage (Fig. 6F). Also, in the observable nuclei, *unc-6* reporter intensity was reduced at A3 compared with L4 (Fig. 6G). For example, the intensity in M1 muscle dropped significantly at the A3 stage (***P*<0.01, Mann–Whitney comparison *t*-test) (Fig. 6G). A similar observation was also made in the nuclei of the anterior M8 muscle (Fig. 6G).

To test whether the *unc-6* expression is regulated by IIS, we looked at the expression of the reporter in *daf-2(e1368ts)* and *daf-2(e1368ts); daf-16(lf)* backgrounds. We observed that in a non-permissive temperature, 25°C, the intensity of the reporter in *daf-2(e1368ts)* was significantly higher than that in wild type at the A3 stage (****P*<0.001, Tukey's multiple comparison test) (Fig. 6B,C,H). Next, we found that the intensity of the reporter corresponding to M1, M2 and M8 in *daf-2(e1368ts);daf-16(lf)* was significantly reduced compared with the *daf-2(e1368ts)* single mutant (Fig. 6D,H). Further, we noticed that at the L4 stage, there was a significant decrease in the reporter intensity in *daf-16(lf)* (Fig. 6I). Conversely, the intensity of the reporter was significantly enhanced when *daf-16f* was overexpressed in muscles (Fig. 6E,I). Overall, we concluded that the expression of *unc-6* in muscle is regulated by DAF-16 activity, and this regulation is crucial for the guidance of injured proximal stump towards the VNC.

DISCUSSION

Comprehensively, our work shows that proper guidance and synapse formation during the regrowth of injured PLM axon leads to functional restoration. The role of the chemoattractant Netrin/UNC-6 and its receptor UNC-40/DCC is crucial for ventral guidance of the injured proximal stump. This process is controlled by the DAF-2-DAF-16 axis acting in both neuron and muscle, but not in the intestine. DAF-16 plays an instructive role in upregulating the expression of UNC-40/DCC in injured PLM. DAF-16 also controls the expression of Netrin/UNC-6 in ventral muscles. In *daf-16* mutant, the misguided proximal stump cannot form a synapse-like structure. Therefore, the ventral guidance is an important step in the functional rewiring process in injured PLM neurons (Fig. 7).

Functional rewiring of touch neuron

This study establishes that the axon regrowth of PLM neuron following axotomy can lead to functional restoration irrespective of self-fusion events between injured proximal and distal ends as described previously (Basu et al., 2017; Abay et al., 2017). Functional restoration correlates with the proper guidance of the proximal ends to the VNC and the accumulation of presynaptic proteins, such as RAB-3 and ELKS-1 at the nerve endings. The enrichment pattern of the presynaptic components is comparable to the original synaptic branch. The localization of postsynaptic protein GLR-1 was also observed at the VNC, juxtaposed by the enrichment of the new presynaptic machinery. This is consistent with the previous observation in the lamprey spinal cord that regeneration of new synapse leads to a functional recovery (Oliphint et al., 2010). Another recent study using DA9 motor neuron showed an abnormal accumulation of synaptic proteins in dendrites after axotomy, which did not support functional recovery (Ding and Hammarlund, 2018). Therefore, PLM would be a good system to find the limiting factors in the rewiring process. However, only 40% of the events corresponds to correct targeting at the L4 stage, which further drops to 15% at the A3 stage. This indicates that there are inhibitory components that need further investigation.

It is intriguing that synapse formation at the VNC promotes functional recovery after axonal injury in PLM neuron. This might apparently raise the question of how a chemical synapse can help restore the functional loss, as the electrical synapse to the PVC neuron is sufficient for the behavioral response to posterior touch (Chalfie et al., 1985). Although the gap junction in PLM plays a driving role in the posterior touch response, the chemical connection to AVA was predicted to pause the backward movement upon applying posterior touch stimuli (Chalfie et al., 1985; Bounoutas and Chalfie, 2007). This was further supported by the evidence that the chemical synapse plays an inhibitory role in a tap-response assay (Wicks and Rankin, 1995). Moreover, laser microsurgery of the synaptic branch alone leads to a 30% reduction in touch response (Basu et al., 2017). Therefore, 'ventral targeting' and synapse formation during the regeneration of PLM may help regain the posterior touch sensation.

Insulin signaling controls axon guidance during the functional rewiring

We found that insulin signaling controls the functional restoration after the axotomy of PLM. Loss of insulin receptor *daf-2* or its downstream kinases promotes the functional restoration through enhancement of the 'ventral targeting' events, which is dependent on the FOXO family transcription factor DAF-16. This is consistent with the finding that IIS contributes to the age-dependent decline in growth cone formation during the regeneration of D-type motor neuron (Byrne et al., 2014). However, we found that IIS controls the guidance of regenerating axon irrespective of age, and that DAF-16 is essential for proper guidance and functional recovery. A previous study suggested that enhanced regrowth in the *daf-2* mutant is dependent on the MAPKKK dual leucine zipper kinase-1 and that the expression of *dlk-1* is driven by transcriptional activity of DAF-16 (Byrne et al., 2014). Our data indicate that although DLK-1 is sufficient to promote the regrowth of injured axon, it does not support accuracy in the regrowth. Therefore, we identified a DLK-1-independent step in axon regeneration that is highly coordinated by the axon guidance molecules. We provided evidence that DAF-16 regulates the expression of UNC-40 and UNC-6 in neuron and muscle, respectively. This is also consistent with the previous finding that UNC-6 is required for the accuracy of the post-injury regrowth of AVM neuron (Gabel et al., 2008). DAF-16

Development (2021) 148, dev198044. doi:10.1242/dev.198044

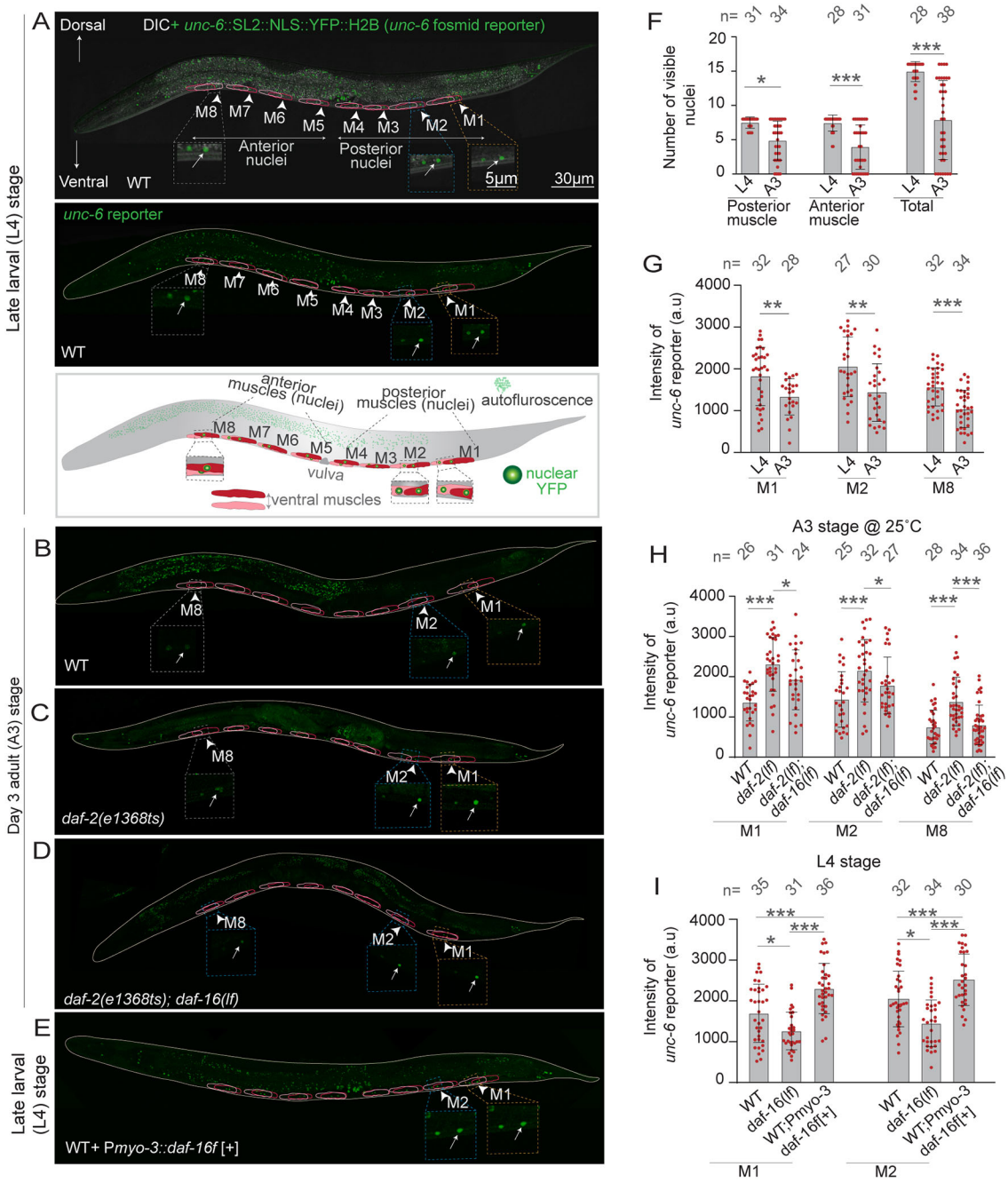

Fig. 6. IIS receptor and DAF-16 regulate unc-6 expression in the ventral muscle. (A) Confocal image with or without the differential interference contrast (DIC) channel of worms at L4 and A3 stages showing the expression of *unc-6(fosmid)::SL2::NLS::YFP::H2B* in the nuclei of ventral muscles (arrowheads) shown as M1 to M8. (B-D) Confocal images showing *unc-6* expression in wild type (WT) (B), *daf-2(e1368ts)* (C) and *daf-2(e1368ts); daf-16(lf)* (D) in day 3 (A3) adults. (E) The expression of *unc-6* in the background of the P*myo-3::daf-16f* [*shrEx313*] transgene at L4 stage. The insets show the enlarged images of the nuclei of M1, M2 and M8 muscles. The ventral muscles are shown using the dark and light red color outlines. (F) The number of visible nuclei showing the localization of *unc-6*::YFP at L4 and A3 stages. *N* (independent replicates)=3-5. (G) The mean intensity of *unc-6*::YFP reporter in nuclei of M1, M2 and M8 muscles at L4 and A3 stages. *N*=3-5. (H) The mean intensity of *unc-6* reporter in the nuclei of M1, M2 and M8 muscles in wild-type, *daf-2(e1368ts)* and *daf-2(e1368ts); daf-16(mu86)* worms imaged at the A3 stage. *N*=4-7. (I) The mean intensity of UNC-6::YFP in the nuclei of M1 and M2 muscles in wild-type, *daf-16(lf)* and P*myo-3*::*daf-16f* (*shrEx313*) backgrounds. *N*=3-6. Data are mean±s.d. **P*<0.05; ***P*<0.01; ****P*<0.001; ns, non-significant [Mann–Whitney unpaired non-parametric two-tailed Student's *t*-test (F,G); ANOVA with Tukey's multiple comparisons test (H,I)]. a.u., arbitrary units.

plays several roles in neurodevelopment, including axon growth (Christensen et al., 2011; Kennedy et al., 2013; Grossman et al., 2013) and neuronal migration (Kennedy et al., 2013) in both a cell-autonomous and non-autonomous manner. It is also required for neuronal remodeling due to hypoxia (Pocock and Hobert, 2008) and food deprivation (Calixto et al., 2012; Caneo et al., 2019).

DAF-16 regulates the expression of axon guidance molecules during regeneration

We were intrigued to find that DAF-16 is required for the 'ventral targeting' of the PLM axon during regeneration, irrespective of DAF-2. The promoter of the *unc-40* gene has a binding site for DAF-16 (Gerstein et al., 2010; Celniker et al., 2009). We found that

Development (2021) 148, dev198044. doi:10.1242/dev.198044

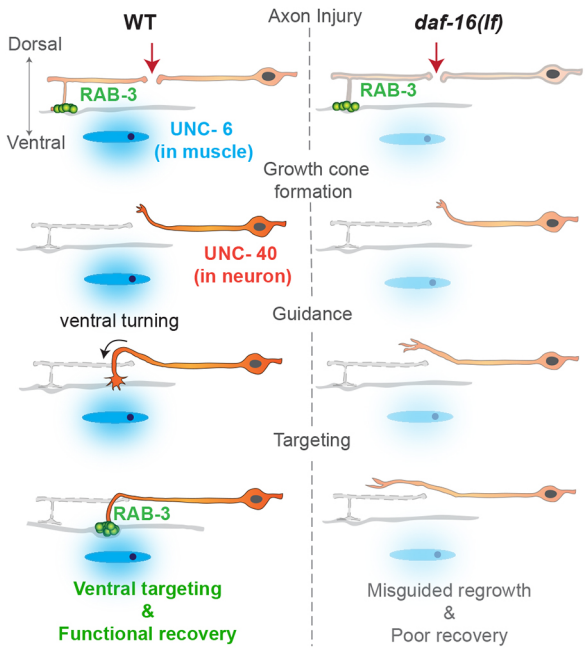

Fig. 7. Model demonstrating how the guidance of the injured PLM axon towards the ventral cord is compromised in *daf-16* mutant due to lack of expression of UNC-40 and UNC-6 in neuron and muscle, respectively.

the DAF-16 promotes the expression of UNC-40 after axotomy. How might DAF-16 be regulated upon axonal injury? A previous study indicated that in response to heat stress, C-Jun-N terminal kinase-1 (JNK-1) helps in the translocation of DAF-16 to the nucleus and extends lifespan in a pathway parallel to IIS (Oh et al., 2005). Moreover, the JNK-1 MAP kinase pathway is required for axon regeneration in *C. elegans* (Li et al., 2012; Nix et al., 2014). Upon axon injury, JNK-1/DLK-1 gets activated by local injury signal, such as cAMP (Hao et al., 2016); therefore, it can activate DAF-16.

Axon guidance cues are often modulated to improve axon regeneration after traumatic injury in the central and peripheral nervous system (Giger et al., 2010; Becker and Becker, 2007). The expression and localization pattern of these cues are different in adulthood as opposed to the pattern seen during early development (Hilton and Bradke, 2017). These cues are expressed aberrantly after the lesion of the nervous system (Giger et al., 2010; Chen et al., 2020; Dun and Parkinson, 2017). Both Netrin and Slit play important roles in axon regeneration after sciatic nerve transection (Dun et al., 2019). Recently, it has been seen that following axon injury, *let-7* miRNA negatively regulates the expression of *slit* and *dcc* in peripheral neurons (Wang et al., 2019). Our finding gives novel insight into the regulation of axon guidance ligands and receptors by DAF-16.

MATERIALS AND METHODS

Genetics and *C. elegans* strains

C. elegans strains were grown on nematode growth medium (NGM) agar plates at 20°C using standard methods (Brenner, 1974). The loss-of-function alleles were denoted as '*lf*' throughout the paper except for the *daf-2* mutant. In this study, we used two temperature-sensitive alleles of *daf-2*. One of them is *daf-2(e1368ts)*, and the other is *daf-2(m596ts)*. Both *daf-2(e1368ts)* and *daf-2(m596ts)* mutants were grown in permissive temperature at 20°C. When L2 staged larva of these mutants are transferred to the non-permissive temperature of 25°C they produce Dauer larvae (Riddle et al., 1981). This characteristic was used to make single and double mutants involving *daf-2(lf)*. All the strains used in the study are described in Table S2. The strains containing the newly generated transgenic extrachromosomal arrays are mentioned in Table S3.

Femtosecond lasers and axotomy

The axotomy experiments were performed either at the late larval (L4) stage or with 3-day-old adult worms (A3 stage). During axotomy experiments, the worms were immobilized using 0.2 µl of 0.1 µm diameter polystyrene beads (Polysciences, 00876-15) in 5% agarose pads (Basu et al., 2017). Axotomy and imaging were performed using a Bruker Ultima two-photon microscope (Basu et al., 2017). The 60× water immersion objective (NA= 1.1) was used for imaging and axotomy of PLMs. The laser wavelengths of 920 nm and 1020 nm were used for imaging the GFP- and mScarlet-labeled PLMs, respectively. The laser wavelength of 720 nm was used for cutting the axon (Fig. 1A). The cutting laser was set at a pulse width of ∼80 fs, an irradiation pulse width of 20 ms, a lateral point spread function (PSF) of ∼400 nm, and a *z*-axis PSF of ∼1.5 µm. For most of the experiments, both the PLM axons located on the left and right sides of the worm were severed, unless otherwise mentioned. The gentle touch response assay was then performed at 3 h and 24 h or 48 h post-axotomy (Fig. 1A). Usually, two small cuts of 6 µm apart were introduced at a 50 µm distance from the cell body of PLM (Fig. 1A; Basu et al., 2017).

Gentle touch assay and recovery index

The gentle touch response assay (Chalfie et al., 2014; Chalfie and Sulston, 1981; Basu et al., 2017) was performed for checking the function related to the PLM neuron before and after axotomy. The PTRI (Chalfie and Sulston, 1981; Chalfie et al., 1985) corresponding to both PLML and PLMR were obtained by performing the assay for the left and right side of the worm, respectively. According to the method described before, the worms were subjected to the anterior and posterior touches alternatively with an eyelash tip (Chalfie et al., 1985, 2014; Chalfie and Sulston, 1981). Anterior touch was given to a forward-moving worm, and a backward-moving animal was subjected to the posterior touch. In response to both the anterior and posterior touches, the worm reverses its direction (Chalfie and Sulston, 1981). A total of ten alternate anterior and posterior touches were given on either side of the worm (Hobert et al., 1999; Chalfie and Sulston, 1981). The response was denoted as '1' and no response as '0' (Basu et al., 2017). The PTRI was quantified as the ratio of the number of responses scored divided by the total number of touches applied. We calculated the PTRI values at 3 h, 24 h and 48 h post-axotomy for each side of the worm. To express the extent of functional recovery quantitatively, we divided the PTRI value measured at 24 h or 48 h post-axotomy by the PTRI obtained just after axotomy (3 h post-axotomy). The functional recovery was defined as the RI (Fig. 1D; Fig. S1A). Therefore, an RI value above 1 (green dashed line, Fig. 1D) denotes successful functional recovery.

Correlation of RI with the axon regeneration pattern

For correlating the RI corresponding to a given side of the worm with the regrowth pattern, we imaged the regeneration event from the same side using a point-scanning confocal microscope LSM510 Meta (Zeiss) after the touch response assay was conducted at 24 h or 48 h post-axotomy (Fig. 1A). The worms were mounted on a 5% agarose pad with 10 mM levamisole hydrochloride (Sigma-Aldrich, L0380000) for imaging (Fig. 1A). Typically *z*-sections were scanned at 0.5 µm intervals under a 63× oil objective (NA=1.46). Approximately 56% of 480 nm laser and 68% of 543 nm laser were used for imaging the *muIs32* [P*mec-7*-GFP] and *shrEx209* [P*mec-4*-mScarlet] reporters, respectively. The captured *z*-slices were pseudocolored using ImageJ (Fiji) to represent the depth across the *z*-sections (Fig. 1C). Broadly, the regrowth patterns were divided into 'fusion' and 'non-fusion' events (Fig. 1A). The axons categorized in the 'non-fusion' class followed different trajectories of regrowth (Fig. 1C). The 'non-fusion' category was further classified into two subcategories, 'ventral targeting' events (Fig. 1Ca,Cb) and 'non-ventral' regrowth (Fig. 1Cc,Cd). The PLM neuron has a ventral branch (arrowhead, Fig. 1A), which makes synapse onto the postsynaptic interneuron (Fig. 1A,F; Chen et al., 2017). This allowed us to set the dorsal-ventral axis of the worm (Fig. 1A) while analyzing the direction of regrowth at 24 h or 48 h post-axotomy. The axons

Development (2021) 148, dev198044. doi:10.1242/dev.198044

that regrew up to 35-45 µm depth in a ventral direction and fasciculated along the VNC were characterized as 'ventral targeting' events, whereas the axons regrowing up to the same depth in the dorsal direction were identified as 'dorsal targeting' events. When multiple branches emanated from the cut tip, the event was named as a 'multibranch' event. When the proximal stump regrew straight towards the anterior side without any deviation ('non-fusion' event in Fig. 1A), it was termed as 'straight regrowth'.

Quantitative analysis of axon regrowth

First, the optical sections corresponding to a regeneration event were projected together. Then, the longest neurite length was measured from the cell body to the tip of the regenerated axon. To calculate the actual regrowth length at 24 h or 48 h post-axotomy, the distance from the cell body to the injury site was measured and subtracted from the distance between the cell body and the regrowth tip. We used Image J for calculating the regrowth length of the regenerated PLM axon. The total fasciculation along the ventral cord (Double-headed yellow arrows, Fig. 2E) corresponding to the 'ventral targeting' events was measured as 'longitudinal regrowth along the VNC' (Fig. 2F).

Experiments with the temperature-sensitive *daf-2* mutants

For the experiments related to the temperature-sensitive *daf-2* mutants, the wild-type and mutant worms were grown at the permissive temperature of 20°C until L4 stage, and were then transferred at a non-permissive temperature of 25°C for 3 days to obtain A3 stage (day-3 old) worms for axotomy experiments. After axotomy was performed, the worms were transferred back to 25°C for 24 h or 48 h before the assessment of PTRI and imaging. For performing the experiments with *daf-2(e1368ts)* mutants at the L4 stage, L3-staged worms were transferred from 20°C to 25°C and were allowed to grow until late L4 stage before the quantitative imaging of UNC-40-GFP intensity in PLM (Fig. 5D-G; Fig. S4D-G).

Molecular biology and transgenes

For the tissue-specific expressions of *daf-16f* and *daf-16a* isoforms, we first prepared gateway (Thermo Fisher Scientific) entry clones of *daf-16f* and *daf-16a*. We obtained the *daf-16* cDNAs from the Yuji Kohara cDNA consortium (https://nematode.nig.ac.jp/dbest/keysrch.html). pCR8::*daf-16f* (NBRGWY106) and pCR8::*daf-16a* (NBRGWY96) were prepared by PCR8 cloning. For making pCR8::*daf-16f* (NBRGWY106), PCR was performed with the primers 5′-GACATGCAAGCGTGGAACTGTCGTG-3′ and 5′-TGATGATTTAATAAAAATCAAATTTGG-3′, using *daf-16f* cDNA (yk3444n05) as the template, followed by ligation into the pCR8/GW/TOPO vector (Thermo Fisher Scientific, K2500-20). Similarly, for making pCR8::*daf-16a* (NBRGWY96), PCR was performed with the primers 5′-GGATGAACGACTCAATAGACGACG-3′ and 5′ TGATGATTTAATAAAAATCAAATTTGG-3′ using *daf-16a* cDNA (yk3193h05) as a template. The pCR8 plasmids were recombined with PCZGY553 [P*mec-4*::Gateway destination vector], PCZGY925 [P*myo-3*::Gateway destination vector], PCZGY44 [P*dpy-7*::Gateway destination vector] and PCZGY66 [P*rgef-1*::Gateway destination vector] using LR clonase (Thermo Fisher Scientific, K2500-20) for expressing *daf-6a/f* in touch neuron, muscle, epidermal cells and all the neurons, respectively. These plasmids were injected either into wild-type or *daf-16(lf)* background with a concentration of 10 ng/µl. The *pttx3*-RFP was used as a co-injection plasmid at a concentration of 40 ng/µl mixed with the pBSK (105-110 ng/µl). To make P*mec-4*-mScarlet, first, the coding sequence of mScarlet was amplified using primers 5′-GGCTGCTCTTCGATGGTCTC-3′ and 5′-CTGGGTGCTCTTCGCTACTTGTAG-3′, using Addgene plasmid pMS050 as a template, followed by ligation into pCR8/GW/TOPO. pCR8::mScarlet (PNBRGWY52) was recombined with pCZGWY553 [P*mec-4*::Gateway destination vector] using LR Clonase to obtain P*mec-4*::mScarlet (PNBRGWY54). PNBRGWY54 was injected at a concentration of 5 ng/µl along with 40 ng/µl of pttx3::RFP plasmid as the co-injection marker and 120 ng/µl of pBSK plasmid in the N2 strain to make P*mec-4*::mScarlet containing transgenic worms. pCR8::dlk-1 (PNBRGWY14) was recombined with pCZGWY553 [P*mec-4*::Gateway destination vector] using LR Clonase to construct P*mec-4*::*dlk-1* (PNBRGWY13). PNBRGWY13 was injected at a concentration of 0.5 ng/µl along with 40 ng/µl of pttx3::RFP plasmid as the co-injection marker and 120 ng/µl of pBSK plasmid in wild-type and *daf-16(lf)* strains.

Analysis of mRNA sequencing data in *daf-16* mutant

Comparative transcriptomics data of *daf-2(lf)* and *daf-2(lf); daf-16(lf)* from Kaletsky et al. (2016) were analyzed using an enrichment analysis tool (www.wormbase.org/tools/enrichment/tea/tea.cgi) (Angeles-Albores et al., 2016). The q value threshold was kept as 0.1 (Kaletsky et al., 2016). Fold change values of relevant GO term genes were analyzed and interpreted. Transcriptomics data from Kaletsky et al. (2016) showed differential expression of ∼9000 neuronal genes. We further applied the GO term (GO: 0097485) relevant to neuronal projection and guidance and found ∼110 genes (Table S4).

Imaging and quantitative analysis of GFP/mCherry::RAB-3 intensity

The worms were immobilized on a 5% agarose pad with 10 mM levamisole. The *jsIs821* [P*mec-7*::GFP::RAB-3] (Luo et al., 2014; Mondal et al., 2011) and *shrEx209* [P*mec-4*::mScarlet] reporters were simultaneously imaged using a LSM510 Meta confocal microscope (Zeiss) before and 24 h after axotomy. The confocal planes were scanned at 0.5 µm intervals under a 63× oil objective (NA=1.46). Approximately 65% of 488 nm laser and 70.2% of 543 nm laser were used for imaging the GFP::RAB-3 and mScarlet reporters, respectively. The mean intensity of GFP::RAB-3 and mScarlet was measured from the ROI of 3 µm drawn at the tip of the regrowing axon (Fig. 1E; Fig. S1B). To quantify the GFP::RAB-3 intensity at the synaptic region of the ventral branch, a similar ROI was placed at the ventral cord region at the end of the branch (Fig. 1F). The mean intensity was quantified from the *z*-stacked image after background subtraction using the Image J. For comparing the GFP::RAB-3 intensities across various regrowth events, GFP::RAB-3 intensity was normalized by the mean intensity of mScarlet from the same ROI (Fig. 1E,F). Similarly, P*mec-4::*mcherry*::*RAB-3 *(tbIs227)* reporter (Sood et al., 2018) in *muIs32* (P*mec-7*::GFP) background was used to image the different regrowth events at L4 and A3 stages at 24 h post-axotomy (Fig. 2E,G). The simultaneous imaging of the PLM neuron expressing *muIs32* and *tbIs227* (P*mec-4*::mCherry::RAB-3) was performed using a 60× oil objective (NA=1.4) of a Nikon A1 plus confocal microscope at 0.5 µm slice intervals. Approximately 0.8% of 488 nm laser and 1% of 543 nm laser were used for imaging the *muIs32* and P*mec-4*::mCherry::RAB-3 *(tbIs227)* reporters, respectively. For correlating the recovery indices (Fig. S1C; Fig. S2B) to the GFP/mCherry::RAB-3 localization, the touch response assay was performed before proceeding with the confocal imaging.

Imaging and quantitative analysis of the UNC-40::GFP-reporter

The PLM neuron expressing *icIs132* [P*unc-40*::UNC-40::GFP] (Chan et al., 1996) and *shrEx209* [P*mec-4*-mScarlet] was imaged using a Zeiss LSM510 Meta confocal microscope in the wild-type, *daf-2(e1368ts)* and *daf-16(lf)* backgrounds. Images were collected before and at 0 h, 3 h, 5 h and 8 h post-axotomy. Three to five *z* slices were taken at a 0.5 µm interval using a 63× oil objective (NA=1.46). Three planes were *z* projected for the quantification of UNC-40::GFP and mScarlet from PLM cell body. With regards to the axon tip, the number of *z* slices that were imaged became higher depending on the extent of regrowth. Approximately 18% of 488 nm laser and 65.5% of 543 nm laser were used for imaging the UNC-40::GFP and mScarlet reporters, respectively. Detector gains used for imaging with 488 nm and 543 nm lasers were 685 and 732, respectively. We captured the images in 8 bits. Therefore, the saturation limit for the image intensities was 256 arbitrary units for both 488 nm and 561 nm lasers. The images were collected below the saturation limit (Fig. S4D-G). The mean intensity of UNC-40::GFP and mScarlet in the PLM cell body were determined from an ROI surrounding the cell body (Fig. 5D). The mean intensity in the axon was measured from a line ROI of 5 µm length placed at 50 µm distance (Fig. 5E) from the cell body (before axotomy) or the tip of the regenerating axon (Fig. 5E,G). The background intensities were determined from the same ROIs placed inside the worm away from PLM. The background correction was performed before determining the normalized intensities (Fig. 5F,G).

ELKS-1::tag RFP imaging

PLM neuron expressing *muIs32* [P*mec-7*::GFP] and *jsIs1075* [P*mec-7*-TagRFP::ELKS-1] (Zheng et al., 2014) reporter was imaged using a Zeiss LSM 510 Meta confocal microscope at 24 h post-axotomy (Fig. S1D). Confocal planes were imaged at 0.5 µm *z* intervals under a 40× air objective (NA=0.75). The excitation laser powers were 66% and 78% for 488 nm and 543 nm, respectively. Detector gains were 650 and 738 for 488 nm and 543 nm lasers, respectively.

GLR-1::GFP imaging

PLM neuron expressing *shrEx209* [P*mec-4*::mScarlet] and AVA neuron expressing *akIs141* [P*rig3*::GLR1::GFP] reporter (Hoerndli et al., 2015) were imaged using a Nikon A1 plus confocal microscope at 24 h post-axotomy (Fig. S1E). Confocal planes were scanned at 1 µm intervals under a 60× oil objective (NA=1.4). Excitation power was at 5% and 0.5% for 488 nm and 561 nm lasers, respectively.

unc-6 (fosmid):: SL2::NLS::YFP::H2B imaging

The *unc-6* reporter (*OtIs638*) [*unc-6* (fosmid):: NLS::YFP::H2B] (Weinberg et al., 2018) was imaged in wild-type, *daf-2*(*e1368ts*), *daf-2(e1368ts);daf-16(lf)* and *Pmyo-3::daf-16f* (*shrEx314*) backgrounds using a Nikon A1 plus confocal microscope (Fig. 6A-E). Images were captured using a 60× oil objective (NA=1.4) at 2-µm *z*-section intervals. Approximately 5% 488 nm laser power was used to image *unc-6*(fosmid)::YFP and 2% 561 nm laser power was used for imaging red fluorescence. We captured the images in 12 bits. Therefore, the saturation limit is 4096 arbitrary units for both 488 nm and 561 nm lasers (Fig. 6G-I). Approximately 10 to 12 *z* planes were merged for collecting the intensity from all eight pairs of muscle nuclei. The four pairs of muscle nuclei from anal region to vulva are termed as M1, M2, M3 and M4. The other four pairs of nuclei expanding from vulva to pharynx are named as M5, M6, M7 and M8 (Fig. 6A). To remove the autofluorescence, we subtracted the *z*-projected image of the red channel (561 nm) from the *z*-projected image of the green channel (488 nm). The mean intensity of the *unc-6* reporter was determined from a circular ROI of 2 µm radius surrounding the nuclei M1, M2 and M8 (Fig. 6A-E) after background correction. The images were collected below the saturation limit.

Experiments related to ageing

The worms at the L4 stage were transferred to OP50-seeded 60 mm NGM plates containing 50 mM of 5′ fluro-2′deoxyuridine (FuDR; Sigma-Aldrich, F0503) (Sutphin and Kaeberlein, 2009). The presence of food was monitored every 2 days. If the food became a little less, the worms were transferred to a newly seeded plate. The number of living worms and dead worms was calculated every day as the L4 s were transferred for lifespan determination. This counting of worms was carried out until and unless there were no living animals. Before performing axotomy of age-related mutants, we verified whether the lifespan of these mutants in our growth condition matched with the previous studies (Berman and Kenyon, 2006).

Statistics

Statistical analysis for all experiments in this paper was conducted using GraphPad Prism (GraphPad Prism 8.2.1). Three or more arrays were compared using ANOVA (non-parametric) with Tukey's multiple comparisons test. Two conditions were compared using a Mann–Whitney *t*-test (non-parametric). Fisher's exact test was used to compare the percentage values of multiple sets in the contingency plots. For all the plots, '*n*' (the number of samples) and '*N*' (the number of independent replicates) are mentioned in the figure panels and the legends, respectively. Data are mean±s.d.

Acknowledgements

We thank Yuji Kohara for cDNAs; the National BioResource Project, Japan; and the *Caenorhabditis* Genetics Center (CGC) for strains. The CGC is supported by the National Institutes of Health Office of Research Infrastructure Programs (P40 OD010440). We also thank Keerthana Ponniah for cloning and strain constructions; Bhavani Shankar Sahu, Swagata Dey and Arnab Mukhopadhyay for their comments on the manuscript; and A Mukhopadhyay, S. P. Koushika, K. Babu and M. Nonet for help with strains.

Competing interests

The authors declare no competing or financial interests.

Author contributions

Conceptualization: A.B., A.G.-R.; Methodology: A.B., S. Bhardwaj, S.D.; Software: S.D.; Formal analysis: A.B., S. Behera; Investigation: A.B., S. Behera; Resources: A.B., S. Behera, S. Bhardwaj, A.G.-R.; Writing - original draft: A.B., A.G.-R.; Visualization: A.B., S. Behera; Supervision: A.G.-R.; Project administration: A.G.-R.; Funding acquisition: A.G.-R.

Funding

This work was supported by the National Brain Research Centre core fund from the Department of Biotechnology, DBT/Wellcome Trust India Alliance (IA/I/13/1/500874 to A.G.-R.) and the Science and Engineering Research Board (CRG/2019/002194 to A.G.-R.). A.G.-R. is an intermediate fellow of DBT/Wellcome Trust India Alliance. Deposited in PMC for release after 6 months.

Peer review history

The peer review history is available online at https://journals.biologists.com/dev/article-lookup/doi/10.1242/dev.198044

References

Abay, Z. C., Wong, M. Y.-Y., Teoh, J.-S., Vijayaraghavan, T., Hilliard, M. A. and Neumann, B. (2017). Phosphatidylserine save-me signals drive functional recovery of severed axons in Caenorhabditis elegans. *Proc. Natl. Acad. Sci. USA* **114**, E10196-E10205. doi:10.1073/pnas.1703807114

Alam, T., Maruyama, H., Li, C., Pastuhov, S. I., Nix, P., Bastiani, M., Hisamoto, N. and Matsumoto, K. (2016). Axotomy-induced HIF-serotonin signalling axis promotes axon regeneration in C. elegans. *Nat. Commun.* **7**, 10388. doi:10.1038/ncomms10388

Angeles-Albores, D., Lee, R. Y. N., Chan, J. and Sternberg, P. W. (2016). Tissue enrichment analysis for C. elegans genomics. *BMC Bioinformatics* **17**, 366. doi:10.1186/s12859-016-1229-9

Asakura, T., Waga, N., Ogura, K.-I. and Goshima, Y. (2010). Genes required for cellular UNC-6/netrin localization in Caenorhabditis elegans. *Genetics* **185**, 573-585. doi:10.1534/genetics.110.116293

Bansal, A., Zhu, L. J., Yen, K. and Tissenbaum, H. A. (2015). Uncoupling lifespan and healthspan in Caenorhabditis elegans longevity mutants. *Proc. Natl. Acad. Sci. USA* **112**, E277-E286. doi:10.1073/pnas.1412192112

Basu, A., Dey, S., Puri, D., Das Saha, N., Sabharwal, V., Thyagarajan, P., Srivastava, P., Koushika, S. P. and Ghosh-Roy, A. (2017). let-7 miRNA controls CED-7 homotypic adhesion and EFF-1-mediated axonal self-fusion to restore touch sensation following injury. *Proc. Natl. Acad. Sci. USA* **114**, E10206-E10215. doi:10.1073/pnas.1704372114

Becker, C. G. and Becker, T. (2007). Growth and pathfinding of regenerating axons in the optic projection of adult fish. *J. Neurosci. Res.* **85**, 2793-2799. doi:10.1002/jnr.21121

Becker, T., Wullimann, M. F., Becker, C. G., Bernhardt, R. R. and Schachner, M. (1997). Axonal regrowth after spinal cord transection in adult zebrafish. *J. Comp. Neurol.* **377**, 577-595. doi:10.1002/(SICI)1096-9861(19970127)377:4<577::AID-CNE8>3.0.CO;2-#

Bei, F., Lee, H. H. C., Liu, X., Gunner, G., Jin, H., Ma, L., Wang, C., Hou, L., Hensch, T. K., Frank, E. et al. (2016). Restoration of Visual Function by Enhancing Conduction in Regenerated Axons. *Cell* **164**, 219-232. doi:10.1016/j.cell.2015.11.036

Benowitz, L. I. and Popovich, P. G. (2011). Inflammation and axon regeneration. *Curr. Opin. Neurol.* **24**, 577-583. doi:10.1097/WCO.0b013e32834c208d

Berman, J. R. and Kenyon, C. (2006). Germ-cell loss extends C. elegans life span through regulation of DAF-16 by kri-1 and lipophilic-hormone signaling. *Cell* **124**, 1055-1068. doi:10.1016/j.cell.2006.01.039

Blanquie, O. and Bradke, F. (2018). Cytoskeleton dynamics in axon regeneration. *Curr. Opin. Neurobiol.* **51**, 60-69. doi:10.1016/j.conb.2018.02.024

Bounoutas, A. and Chalfie, M. (2007). Touch sensitivity in Caenorhabditis elegans. *Pflugers Arch.* **454**, 691-702. doi:10.1007/s00424-006-0187-x

Brenner, S. (1974). The genetics of Caenorhabditis elegans. *Genetics* **77**, 71-94. doi:10.1093/genetics/77.1.71

Brosius Lutz, A. and Barres, B. A. (2014). Contrasting the glial response to axon injury in the central and peripheral nervous systems. *Dev. Cell* **28**, 7-17. doi:10.1016/j.devcel.2013.12.002

Byrne, A. B., Walradt, T., Gardner, K. E., Hubbert, A., Reinke, V. and Hammarlund, M. (2014). Insulin/IGF1 signaling inhibits age-dependent axon regeneration. *Neuron* **81**, 561-573. doi:10.1016/j.neuron.2013.11.019

Calixto, A., Jara, J. S. and Court, F. A. (2012). Diapause formation and downregulation of insulin-like signaling via DAF-16/FOXO delays axonal degeneration and neuronal loss. *PLoS Genet.* **8**, e1003141. doi:10.1371/journal.pgen.1003141

Caneo, M., Julian, V., Byrne, A. B., Alkema, M. J. and Calixto, A. (2019). Diapause induces functional axonal regeneration after necrotic insult in C. elegans. *PLoS Genet.* **15**, e1007863. doi:10.1371/journal.pgen.1007863
Celniker, S. E., Dillon, L. A. L., Gerstein, M. B., Gunsalus, K. C., Henikoff, S., Karpen, G. H., Kellis, M., Lai, E. C., Lieb, J. D., Macalpine, D. M. et al. (2009). Unlocking the secrets of the genome. *Nature* **459**, 927-930. doi:10.1038/459927a
Chalfie, M., Hart, A. C., Rankin, C. H. and Goodman, M. B. (2014). Assaying mechanosensation. In WormBook (ed. The *C. elegans* Research Community). https://doi.org/10.1895/wormbook.1.172.1, http://www.wormbook.org.
Chalfie, M. and Sulston, J. (1981). Developmental genetics of the mechanosensory neurons of Caenorhabditis elegans. *Dev. Biol.* **82**, 358-370. doi:10.1016/0012-1606(81)90459-0
Chalfie, M., Sulston, J. E., White, J. G., Southgate, E., Thomson, J. N. and Brenner, S. (1985). The neural circuit for touch sensitivity in Caenorhabditis elegans. *J. Neurosci.* **5**, 956-964. doi:10.1523/JNEUROSCI.05-04-00956.1985
Chan, S. S.-Y., Zheng, H., Su, M.-W., Wilk, R., Killeen, M. T., Hedgecock, E. M. and Culotti, J. G. (1996). UNC-40, a C. elegans homolog of DCC (Deleted in Colorectal Cancer), is required in motile cells responding to UNC-6 netrin cues. *Cell* **87**, 187-195. doi:10.1016/S0092-8674(00)81337-9
Chen, L., Wang, Z., Ghosh-Roy, A., Hubert, T., Yan, D., O'rourke, S., Bowerman, B., Wu, Z., Jin, Y. and Chisholm, A. D. (2011). Axon regeneration pathways identified by systematic genetic screening in C. elegans. *Neuron* **71**, 1043-1057. doi:10.1016/j.neuron.2011.07.009
Chen, A. T.-Y., Guo, C., Itani, O. A., Budaitis, B. G., Williams, T. W., Hopkins, C. E., Mceachin, R. C., Pande, M., Grant, A. R., Yoshina, S. et al. (2015). Longevity Genes Revealed by Integrative Analysis of Isoform-Specific daf-16/FoxO Mutants of Caenorhabditis elegans. *Genetics* **201**, 613-629. doi:10.1534/genetics.115.177998
Chen, C.-H., He, C.-W., Liao, C.-P. and Pan, C.-L. (2017). A Wnt-planar polarity pathway instructs neurite branching by restricting F-actin assembly through endosomal signaling. *PLoS Genet.* **13**, e1006720. doi:10.1371/journal.pgen.1006720
Chen, B., Carr, L. and Dun, X.-P. (2020). Dynamic expression of Slit1-3 and Robo1-2 in the mouse peripheral nervous system after injury. *Neural Regen. Res.* **15**, 948-958. doi:10.4103/1673-5374.268930
Chisholm, A. D., Hutter, H., Jin, Y. and Wadsworth, W. G. (2016). The genetics of axon guidance and axon regeneration in Caenorhabditis elegans. *Genetics* **204**, 849-882. doi:10.1534/genetics.115.186262
Christensen, R., de la Torre-Ubieta, L., Bonni, A. and Colón-Ramos, D. A. (2011). A conserved PTEN/FOXO pathway regulates neuronal morphology during C. elegans development. *Development* **138**, 5257-5267. doi:10.1242/dev.069062
Ding, C. and Hammarlund, M. (2018). Aberrant information transfer interferes with functional axon regeneration. *eLife* **7**, e38829. doi:10.7554/eLife.38829
Dun, X.-P. and Parkinson, D. B. (2017). Role of Netrin-1 signaling in nerve regeneration. *Int. J. Mol. Sci.* **18**, 491. doi:10.3390/ijms18030491
Dun, X.-P., Carr, L., Woodley, P. K., Barry, R. W., Drake, L. K., Mindos, T., Roberts, S. L., Lloyd, A. C. and Parkinson, D. B. (2019). Macrophage-derived slit3 controls cell migration and axon pathfinding in the peripheral nerve bridge. *Cell Rep.* **26**, 1458-1472.e4. doi:10.1016/j.celrep.2018.12.081
el Bejjani, R. and Hammarlund, M. (2012). Notch signaling inhibits axon regeneration. *Neuron* **73**, 268-278. doi:10.1016/j.neuron.2011.11.017
Fawcett, J. W. (2020). The struggle to make CNS axons regenerate: why has it been so difficult? *Neurochem. Res.* **45**, 144-158. doi:10.1007/s11064-019-02844-y
Fawcett, J. W. and Verhaagen, J. (2018). Intrinsic determinants of axon regeneration. *Dev. Neurobiol.* **78**, 890-897. doi:10.1002/dneu.22637
Fitch, M. T. and Silver, J. (2008). CNS injury, glial scars, and inflammation: inhibitory extracellular matrices and regeneration failure. *Exp. Neurol.* **209**, 294-301. doi:10.1016/j.expneurol.2007.05.014
Gabel, C. V., Antoine, F., Chuang, C.-F., Samuel, A. D. T. and Chang, C. (2008). Distinct cellular and molecular mechanisms mediate initial axon development and adult-stage axon regeneration in C. elegans. *Development* **135**, 1129-1136. doi:10.1242/dev.013995
Geoffroy, C. G., Hilton, B. J., Tetzlaff, W. and Zheng, B. (2016). Evidence for an age-dependent decline in axon regeneration in the adult mammalian central nervous system. *Cell Rep* **15**, 238-246. doi:10.1016/j.celrep.2016.03.028
Gerstein, M. B., Lu, Z. J., van Nostrand, E. L., Cheng, C., Arshinoff, B. I., Liu, T., Yip, K. Y., Robilotto, R., Rechtsteiner, A., Ikegami, K., et al. (2010). Integrative analysis of the Caenorhabditis elegans genome by the modENCODE project. *Science* **330**, 1775-1787. doi:10.1126/science.1196914
Ghosh-Roy, A., Wu, Z., Goncharov, A., Jin, Y. and Chisholm, A. D. (2010). Calcium and cyclic AMP promote axonal regeneration in Caenorhabditis elegans and require DLK-1 kinase. *J. Neurosci.* **30**, 3175-3183. doi:10.1523/JNEUROSCI.5464-09.2010
Giger, R. J., Hollis, E. R., II and Tuszynski, M. H. (2010). Guidance molecules in axon regeneration. *Cold Spring Harb. Perspect. Biol.* **2**, a001867. doi:10.1101/cshperspect.a001867
Graciarena, M., Dambly-Chaudiere, C. and Ghysen, A. (2014). Dynamics of axonal regeneration in adult and aging zebrafish reveal the promoting effect of a first lesion. *Proc. Natl. Acad. Sci. USA* **111**, 1610-1615. doi:10.1073/pnas.1319405111
Grossman, E. N., Giurumescu, C. A. and Chisholm, A. D. (2013). Mechanisms of ephrin receptor protein kinase-independent signaling in amphid axon guidance in Caenorhabditis elegans. *Genetics* **195**, 899-913. doi:10.1534/genetics.113.154393
Hammarlund, M., Nix, P., Hauth, L., Jorgensen, E. M. and Bastiani, M. (2009). Axon regeneration requires a conserved MAP kinase pathway. *Science* **323**, 802-806. doi:10.1126/science.1165527
Hao, Y., Frey, E., Yoon, C., Wong, H., Nestorovski, D., Holzman, L. B., Giger, R. J., Diantonio, A. and Collins, C. (2016). An evolutionarily conserved mechanism for cAMP elicited axonal regeneration involves direct activation of the dual leucine zipper kinase DLK. *eLife* **5**, e14048. doi:10.7554/eLife.14048
He, Z. and Jin, Y. (2016). Intrinsic control of axon regeneration. *Neuron* **90**, 437-451. doi:10.1016/j.neuron.2016.04.022
Hilton, B. J. and Bradke, F. (2017). Can injured adult CNS axons regenerate by recapitulating development? *Development* **144**, 3417-3429. doi:10.1242/dev.148312
Hobert, O., Tessmar, K. and Ruvkun, G. (1999). The Caenorhabditis elegans lim-6 LIM homeobox gene regulates neurite outgrowth and function of particular GABAergic neurons. *Development* **126**, 1547-1562. doi:10.1242/dev.126.7.1547
Hoerndli, F. J., Wang, R., Mellem, J. E., Kallarackal, A., Brockie, P. J., Thacker, C., Madsen, D. M. and Maricq, A. V. (2015). Neuronal activity and CaMKII regulate kinesin-mediated transport of synaptic AMPARs. Neuron **86**, 457–474. doi:10.1016/j.neuron.2015.03.011
Hubert, T., Wu, Z., Chisholm, A. D. and Jin, Y. (2014). S6 kinase inhibits intrinsic axon regeneration capacity via AMP kinase in Caenorhabditis elegans. *J. Neurosci.* **34**, 758-763. doi:10.1523/JNEUROSCI.2886-13.2014
Ishii, N., Wadsworth, W. G., Stern, B. D., Culotti, J. G. and Hedgecock, E. M. (1992). UNC-6, a laminin-related protein, guides cell and pioneer axon migrations in C. elegans. *Neuron* **9**, 873-881. doi:10.1016/0896-6273(92)90240-E
Kaletsky, R., Lakhina, V., Arey, R., Williams, A., Landis, J., Ashraf, J. and Murphy, C. T. (2016). The C. elegans adult neuronal IIS/FOXO transcriptome reveals adult phenotype regulators. *Nature* **529**, 92-96. doi:10.1038/nature16483
Kang, H. and Lichtman, J. W. (2013). Motor axon regeneration and muscle reinnervation in young adult and aged animals. *J. Neurosci.* **33**, 19480-19491. doi:10.1523/JNEUROSCI.4067-13.2013
Kennedy, T. E., Serafini, T., de la Torre, J. R. and Tessier-Lavigne, M. (1994). Netrins are diffusible chemotropic factors for commissural axons in the embryonic spinal cord. *Cell* **78**, 425-435. doi:10.1016/0092-8674(94)90421-9
Kennedy, L. M., Pham, S. C. D. L. and Grishok, A. (2013). Nonautonomous regulation of neuronal migration by insulin signaling, DAF-16/Foxo, and PAK-1. *Cell Rep* **4**, 996-1009. doi:10.1016/j.celrep.2013.07.045
Kim, K. W., Tang, N. H., Piggott, C. A., Andrusiak, M. G., Park, S., Zhu, M., Kurup, N., Cherra, S. J., III, Wu, Z., Chisholm, A. D. and et al. (2018). Expanded genetic screening in Caenorhabditis elegans identifies new regulators and an inhibitory role for NAD(+) in axon regeneration. *eLife* **7**, e39756. doi:10.7554/eLife.39756
Knowlton, W. M., Hubert, T., Wu, Z., Chisholm, A. D. and Jin, Y. (2017). A select subset of electron transport chain genes associated with optic atrophy link mitochondria to axon regeneration in Caenorhabditis elegans. *Front Neurosci* **11**, 263. doi:10.3389/fnins.2017.00263
Kosmaczewski, S. G., Han, S. M., Han, B., IRVING Meyer, B., Baig, H. S., Athar, W., Lin-Moore, A. T., Koelle, M. R. and Hammarlund, M. (2015). RNA ligation in neurons by RtcB inhibits axon regeneration. *Proc. Natl. Acad. Sci. USA* **112**, 8451-8456. doi:10.1073/pnas.1502948112
Laha, B., Stafford, B. K. and Huberman, A. D. (2017). Regenerating optic pathways from the eye to the brain. *Science* **356**, 1031-1034. doi:10.1126/science.aal5060
Li, C., Hisamoto, N., Nix, P., Kanao, S., Mizuno, T., Bastiani, M. and Matsumoto, K. (2012). The growth factor SVH-1 regulates axon regeneration in C. elegans via the JNK MAPK cascade. *Nat. Neurosci.* **15**, 551-557. doi:10.1038/nn.3052
Libina, N., Berman, J. R. and Kenyon, C. (2003). Tissue-specific activities of C. elegans DAF-16 in the regulation of lifespan. *Cell* **115**, 489-502. doi:10.1016/S0092-8674(03)00889-4
Lim, J.-H. A., Stafford, B. K., Nguyen, P. L., Lien, B. V., Wang, C., Zukor, K., He, Z. and Huberman, A. D. (2016). Neural activity promotes long-distance, target-specific regeneration of adult retinal axons. *Nat. Neurosci.* **19**, 1073-1084. doi:10.1038/nn.4340
Liu, Y., Wang, X., Lu, C.-C., Sherman-Kerman, R., Steward, O., Xu, X.-M. and Zou, Y. (2008). Repulsive Wnt signaling inhibits axon regeneration after CNS injury. *J. Neurosci.* **28**, 8376-8382. doi:10.1523/JNEUROSCI.1939-08.2008
Luo, S., Schaefer, A. M., Dour, S. and Nonet, M. L. (2014). The conserved LIM domain-containing focal adhesion protein ZYX-1 regulates synapse maintenance in Caenorhabditis elegans. *Development* **141**, 3922-3933. doi:10.1242/dev.108217
Mahar, M. and Cavalli, V. (2018). Intrinsic mechanisms of neuronal axon regeneration. *Nat. Rev. Neurosci.* **19**, 323-337. doi:10.1038/s41583-018-0001-8
Mondal, S., Ahlawat, S., Rau, K., Venkataraman, V. and Koushika, S. P. (2011). Imaging in vivo neuronal transport in genetic model organisms using microfluidic devices. *Traffic* **12**, 372-385. doi:10.1111/j.1600-0854.2010.01157.x

Murphy, C. T. (2006). The search for DAF-16/FOXO transcriptional targets: approaches and discoveries. *Exp. Gerontol.* **41**, 910-921. doi:10.1016/j.exger.2006.06.040
Murphy, C. T. and Hu, P. J. (2013). Insulin/insulin-like growth factor signaling in C. elegans. In WormBook (ed. The *C. elegans* Research Community), https://doi.org/10.1895/wormbook.1.164.1, http://www.wormbook.org.
Neumann, B., Nguyen, K. C. Q., Hall, D. H., Ben-Yakar, A. and Hilliard, M. A. (2011). Axonal regeneration proceeds through specific axonal fusion in transected C. elegans neurons. *Dev. Dyn.* **240**, 1365-1372. doi:10.1002/dvdy.22606
Nix, P., Hammarlund, M., Hauth, L., Lachnit, M., Jorgensen, E. M. and Bastiani, M. (2014). Axon regeneration genes identified by RNAi screening in C. elegans. *J. Neurosci.* **34**, 629-645. doi:10.1523/JNEUROSCI.3859-13.2014
Oh, S. W., Mukhopadhyay, A., Svrzikapa, N., Jiang, F., Davis, R. J. and Tissenbaum, H. A. (2005). JNK regulates lifespan in Caenorhabditis elegans by modulating nuclear translocation of forkhead transcription factor/DAF-16. *Proc. Natl. Acad. Sci. USA* **102**, 4494-4499. doi:10.1073/pnas.0500749102
Oliphint, P. A., Alieva, N., Foldes, A. E., Tytell, E. D., Lau, B. Y.-B., Pariseau, J. S., Cohen, A. H. and Morgan, J. R. (2010). Regenerated synapses in lamprey spinal cord are sparse and small even after functional recovery from injury. *J. Comp. Neurol.* **518**, 2854-2872. doi:10.1002/cne.22368
Paradis, S. and Ruvkun, G. (1998). Caenorhabditis elegans Akt/PKB transduces insulin receptor-like signals from AGE-1 PI3 kinase to the DAF-16 transcription factor. *Genes Dev.* **12**, 2488-2498. doi:10.1101/gad.12.16.2488
Pocock, R. and Hobert, O. (2008). Oxygen levels affect axon guidance and neuronal migration in Caenorhabditis elegans. *Nat. Neurosci.* **11**, 894-900. doi:10.1038/nn.2152
Rasmussen, J. P. and Sagasti, A. (2017). Learning to swim, again: Axon regeneration in fish. *Exp. Neurol.* **287**, 318-330. doi:10.1016/j.expneurol.2016.02.022
Richardson, C. E. and Shen, K. (2019). Neurite Development and Repair in Worms and Flies. *Annu. Rev. Neurosci.* **42**, 209-226. doi:10.1146/annurev-neuro-070918-050208
Riddle, D. L., Swanson, M. M. and Albert, P. S. (1981). Interacting genes in nematode dauer larva formation. *Nature* **290**, 668-671. doi:10.1038/290668a0
Schaefer, A. M., Hadwiger, G. D. and Nonet, M. L. (2000). rpm-1, a conserved neuronal gene that regulates targeting and synaptogenesis in C. elegans. *Neuron* **26**, 345-356. doi:10.1016/S0896-6273(00)81168-X
Senchuk, M. M., Dues, D. J., Schaar, C. E., Johnson, B. K., Madaj, Z. B., Bowman, M. J., Winn, M. E. and van Raamsdonk, J. M. (2018). Activation of DAF-16/FOXO by reactive oxygen species contributes to longevity in long-lived mitochondrial mutants in Caenorhabditis elegans. *PLoS Genet.* **14**, e1007268. doi:10.1371/journal.pgen.1007268
Sood, P., Murthy, K., Kumar, V., Nonet, M. L., Menon, G. I. and Koushika, S. P. (2018). Cargo crowding at actin-rich regions along axons causes local traffic jams. *Traffic* **19**, 166-181. doi:10.1111/tra.12544
Sutphin, G. L. and Kaeberlein, M. (2009). Measuring Caenorhabditis elegans life span on solid media. *J Vis Exp.* **12**, 1152. doi:10.3791/1152
Taub, D. G., Awal, M. R. and Gabel, C. V. (2018). O-GlcNAc Signaling Orchestrates the Regenerative Response to Neuronal Injury in Caenorhabditis elegans. *Cell Rep* **24**, 1931-1938.e3. doi:10.1016/j.celrep.2018.07.078
Verdú, E., Butí, M. and Navarro, X. (1995). The effect of aging on efferent nerve fibers regeneration in mice. *Brain Res.* **696**, 76-82. doi:10.1016/0006-8993(95)00762-F
Vidal-Sanz, M., Bray, G. M., Villegas-Perez, M. P., Thanos, S. and Aguayo, A. J. (1987). Axonal regeneration and synapse formation in the superior colliculus by retinal ganglion cells in the adult rat. *J. Neurosci.* **7**, 2894-2909. doi:10.1523/JNEUROSCI.07-09-02894.1987
Wang, X., Chen, Q., Yi, S., Liu, Q., Zhang, R., Wang, P., Qian, T. and Li, S. (2019). The microRNAs let-7 and miR-9 down-regulate the axon-guidance genes Ntn1 and Dcc during peripheral nerve regeneration. *J. Biol. Chem.* **294**, 3489-3500. doi:10.1074/jbc.RA119.007389
Weinberg, P., Berkseth, M., Zarkower, D. and Hobert, O. (2018). Sexually Dimorphic unc-6/Netrin Expression Controls Sex-Specific Maintenance of Synaptic Connectivity. *Curr. Biol.* **28**, 623-629.e3. doi:10.1016/j.cub.2018.01.002
White, J. G., Southgate, E., Thomson, J. N. and Brenner, S. (1986). The structure of the nervous system of the nematode Caenorhabditis elegans. *Philos. Trans. R. Soc. Lond. B Biol. Sci.* **314**, 1-340. doi:10.1098/rstb.1986.0056
Wicks, S. R. and Rankin, C. H. (1995). Integration of mechanosensory stimuli in Caenorhabditis elegans. *J. Neurosci.* **15**, 2434-2444. doi:10.1523/JNEUROSCI.15-03-02434.1995
Yan, D., Wu, Z., Chisholm, A. D. and Jin, Y. (2009). The DLK-1 kinase promotes mRNA stability and local translation in C. elegans synapses and axon regeneration. *Cell* **138**, 1005-1018. doi:10.1016/j.cell.2009.06.023
Yanik, M. F., Cinar, H., Cinar, H. N., Chisholm, A. D., Jin, Y. and Ben-Yakar, A. (2004). Neurosurgery: functional regeneration after laser axotomy. *Nature* **432**, 822. doi:10.1038/432822a
Yuan, Y., Kadiyala, C. S., Ching, T.-T., Hakimi, P., Saha, S., Xu, H., Yuan, C., Mullangi, V., Wang, L., Fivenson, E. et al. (2012). Enhanced energy metabolism contributes to the extended life span of calorie-restricted Caenorhabditis elegans. *J. Biol. Chem.* **287**, 31414-31426. doi:10.1074/jbc.M112.377275
Zheng, Q., Ahlawat, S., Schaefer, A., Mahoney, T., Koushika, S. P. and Nonet, M. L. (2014). The vesicle protein SAM-4 regulates the processivity of synaptic vesicle transport. *PLoS Genet.* **10**, e1004644. doi:10.1371/journal.pgen.1004644
Zou, Y., Chiu, H., Zinovyeva, A., Ambros, V., Chuang, C.-F. and Chang, C. (2013). Developmental decline in neuronal regeneration by the progressive change of two intrinsic timers. *Science* **340**, 372-376. doi:10.1126/science.1231321

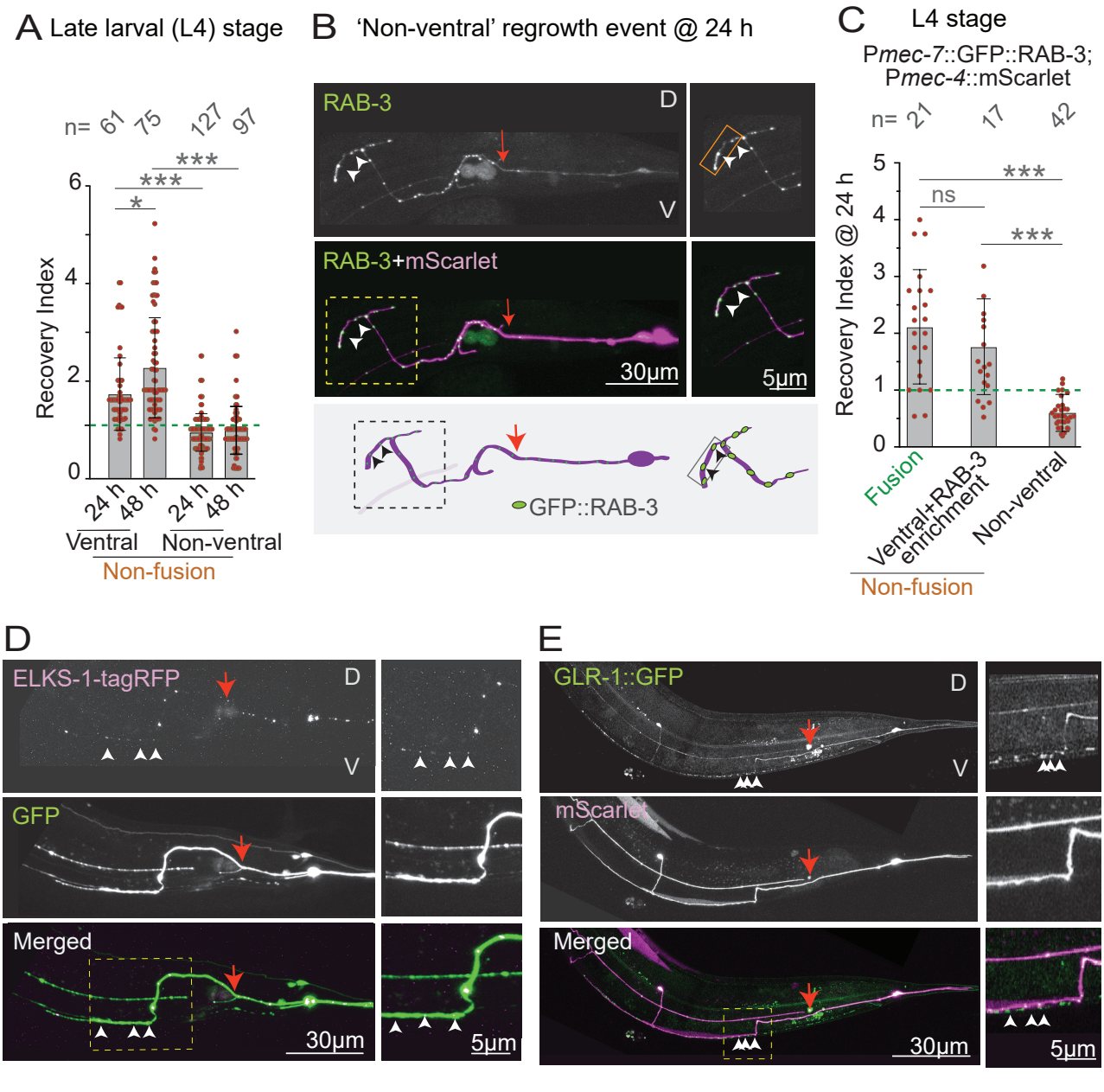

Figure S1: 'Ventral targeting' events often correspond to the enrichment of pre-synaptic reporters at the ventral cord, related to Figure 1.

A) The quantification of the 'Recovery Index' for the 'ventral' and 'non-ventral' regrowth events. N (independent replicates) = 8. B) The confocal image of a 'non-ventral' regrowth event at 24

h postaxotomy of PLM neuron co-expressing the P*mec-7*::GFP::RAB-3 [*jsIs821*] and P*mec-4*::mScarlet [*shrEx209*] reporters. The arrowheads indicate the GFP-RAB-3 punctae localized at the tip of the regrowing axon. The rectangular ROI of 3 µm was used to measure RAB-3 intensity. The red arrow represents the site of injury. C) RI values corresponding to the 'fusion', 'ventral' and 'non-ventral' regrowth events at 24 h postaxotomy in the P*mec-7*::GFP::RAB-3 [*jsIs821*]; P*mec-4*::mScarlet [*shrEx209*] background. N=3-5. D) The confocal image of a 'ventral targeting' event in worm co-expressing P*mec-4*::ELKS-1::tag RFP [*jsIs1075*] and P*mec-7*::GFP [*muIs32*] reporters. The arrowheads indicate the presynaptic enrichment of ELKS-1. E) The confocal image of similar 'ventral targeting' event in worm co-expressing P*rig-3*::GLR-1::GFP [*akIs141*] and *Pmec-4*::mScarlet [*shrEx209*] reporters. The post-synaptic enrichment of GLR-1 is indicated with arrowheads. In A and C, *P < 0.05; ***P < 0.001; ns: non-significant, ANOVA with Tukey's multiple comparisons test. Error bars represent Standard Deviation.

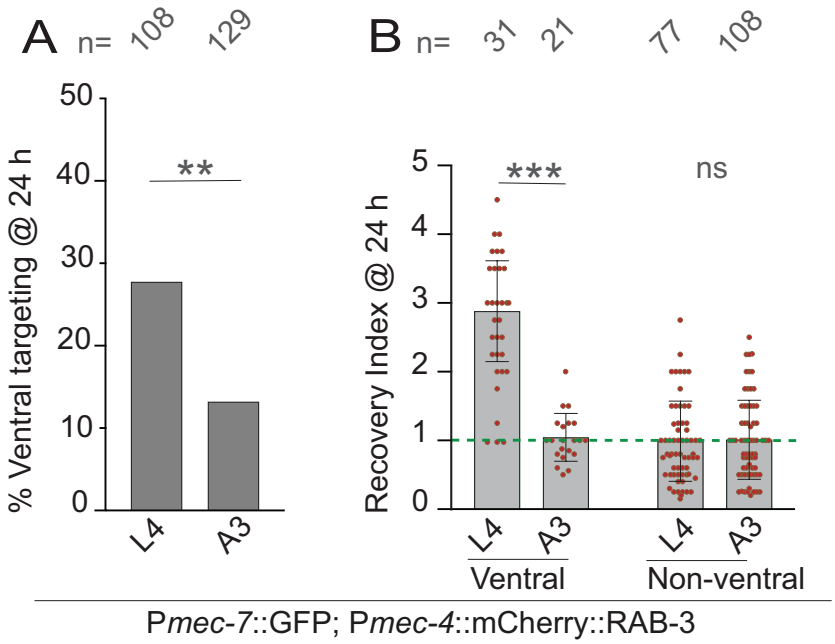

Figure S2: Age related decline in 'ventral targeting' and functional restoration in P*mec-4*:: mCherry::RAB-3 background, related to Figure 2.

A) the percentage of 'ventral targeting' events. B) and RI values corresponding to the different regrowth events in the background expressing P*mec-7*::GFP [*muIs32*] and P*mec-4*::mCherry::RAB-3 [*tbIs227*]. N (independent replicates) = 3-5. In A, **P < 0.01; ns: non-significant; ANOVA with Tukey's multiple comparisons test. In B, ***P < 0.001, Fisher's exact test. Error bars represent Standard Deviation.

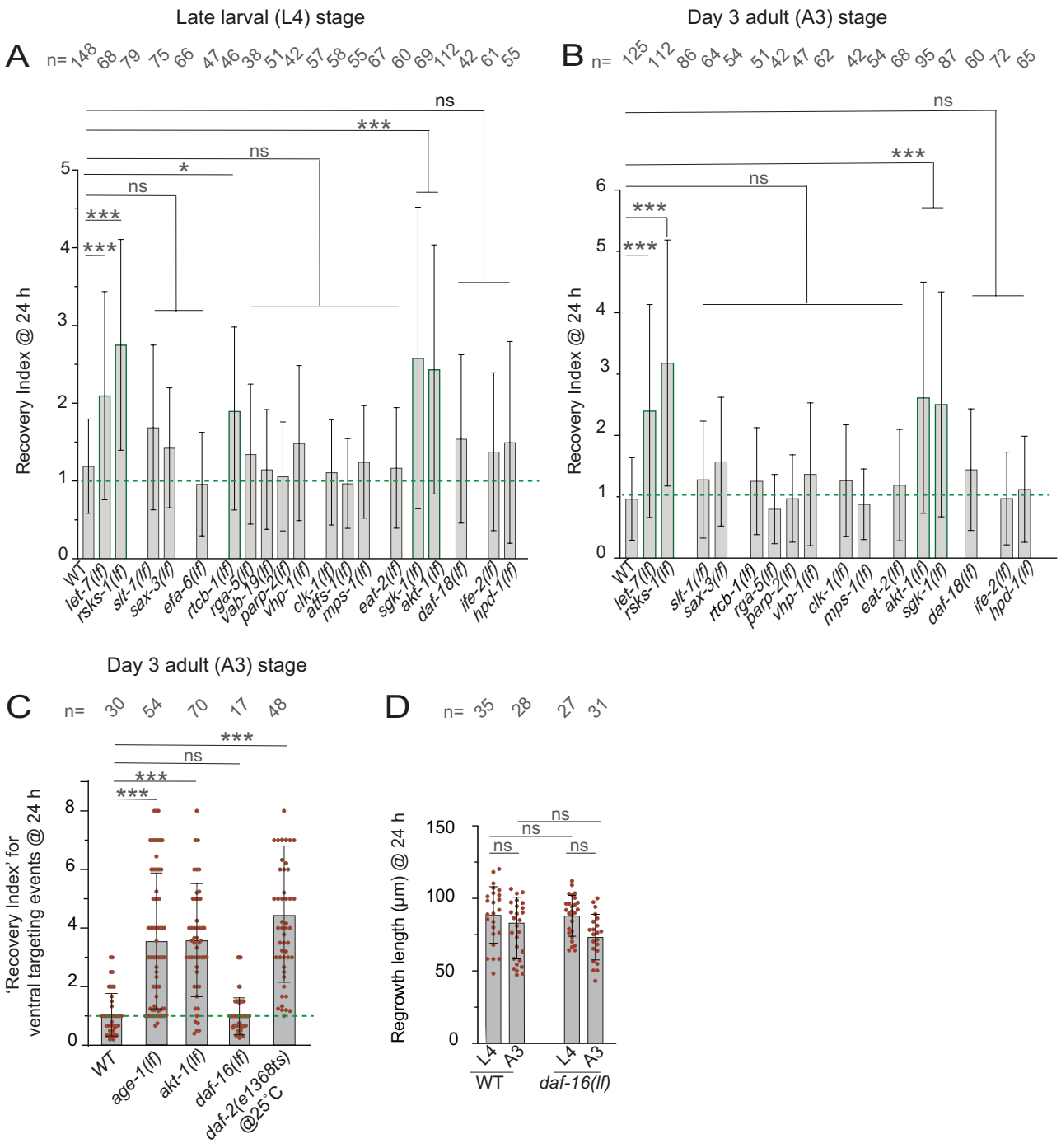

Figure S3: Mutants affecting the Insulin receptor, or the downstream kinases enhances 'ventral targeting' and functional restoration, related to Figure 3.

A-B) The Recovery Index values corresponding to the 'non-fusion' regrowth events in the mutants described in Table S1 at L4 and A3 stages at 24 h postaxotomy**.** N (independent replicates) = 4-8. C) The RI values corresponding to the 'ventral targeting' events in WT and mutants affecting either DAF-2 or downstream kinases at 24 h postaxotomy at A3 stage. N = 5-7. D) The total regrowth length corresponding to the 'non-fusion' events in the WT and *daf-16(lf)* at 24 h postaxotomy. N=3-5. In all plots, *P < 0.05; ***P < 0.001; ns: non-significant; ANOVA with Tukey's multiple comparisons test. Error bars represent Standard Deviation.

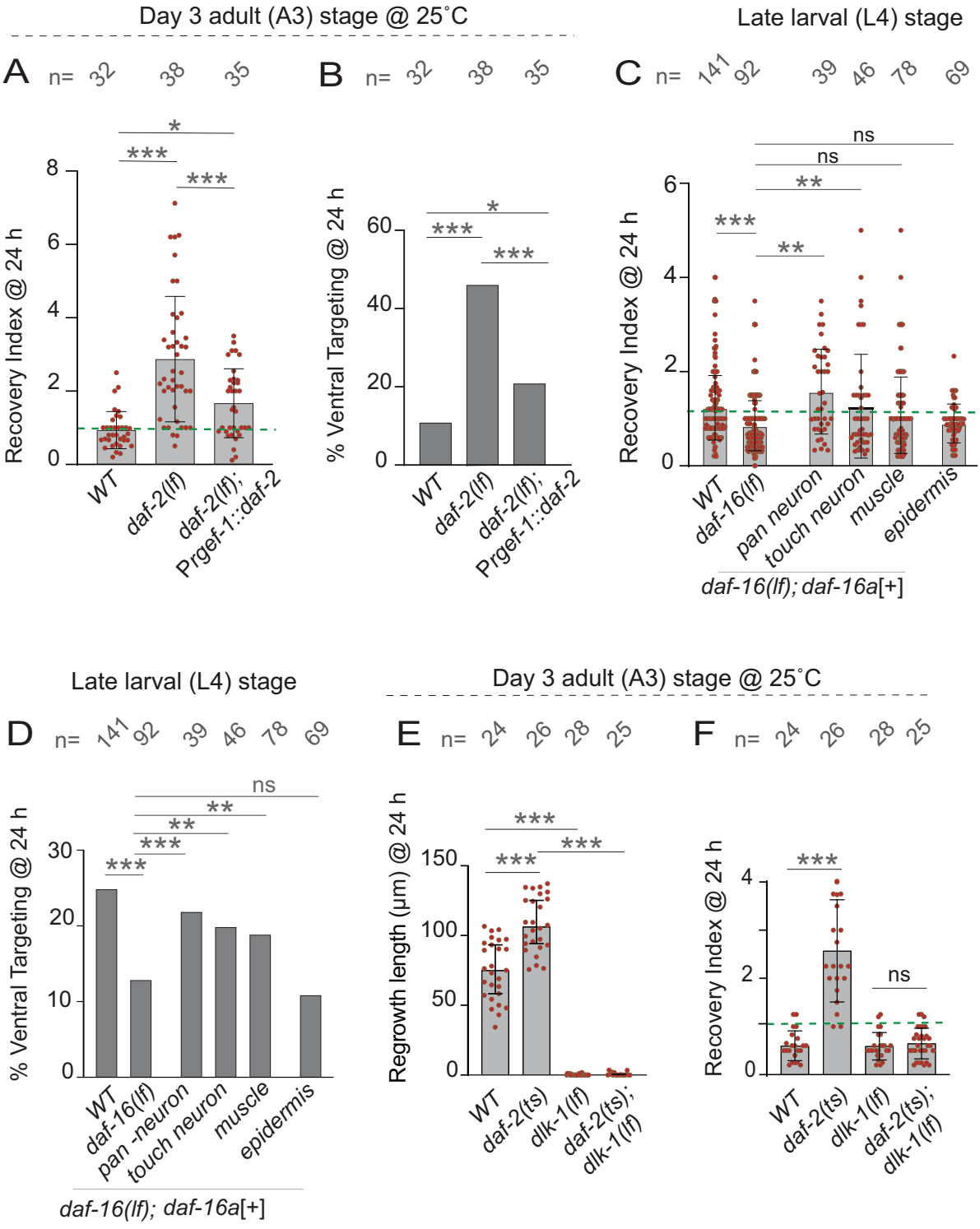

Figure S4: DAF-16 is required both in neuron and muscle for ventral guidance of injured PLM axon, related to Figure 4.

A-B) The quantification of Recovery Index (RI) values (A) and the (%) 'ventral targeting' events (B) corresponding to 'non-fusion' category in WT, *daf-2(m596)* and *daf-2(m596)*; P*rgef-1*::*daf-2* [*hpEx2906*] at 24 h postaxotomy at A3 stage. N (independent replicates) = 3-5. C-D) The RI values (C) and the (%) 'ventral targeting' events (D) corresponding to 'non-fusion' regrowth events in WT, *daf-16(lf)* background with or without the transgene of *daf-16a* expressed under the pan neuronal promoter P*rgef-1* [*shrEx317*], touch neuron-specific promoter P*mec-4* [*shrEx224*], muscle-specific promoter P*myo-3* [*shrEx311*], and the epidermal promoter P*dpy-7* [*shrEx315*]. For both C and D, N=3-5. E-F) The plots show the regrowth length (E) and RI values (F) corresponding to the 'non-fusion' regrowth events at 24 h postaxotomy in WT, *daf-2(e1368ts)*, *dlk-1(lf)* and *daf-2(e1368ts); dlk-1(lf)* backgrounds at A3 stage at 25°C. For both E and F, N= 3. In B and D, *P < 0.05; **P < 0.01; ***P < 0.001; ns: non-significant, Fisher's exact test. In A, C, E and F, *P < 0.05; **P < 0.01; ***P < 0.001; ns: non-significant; ANOVA with Tukey's multiple comparisons test. Error bars represent Standard Deviation.

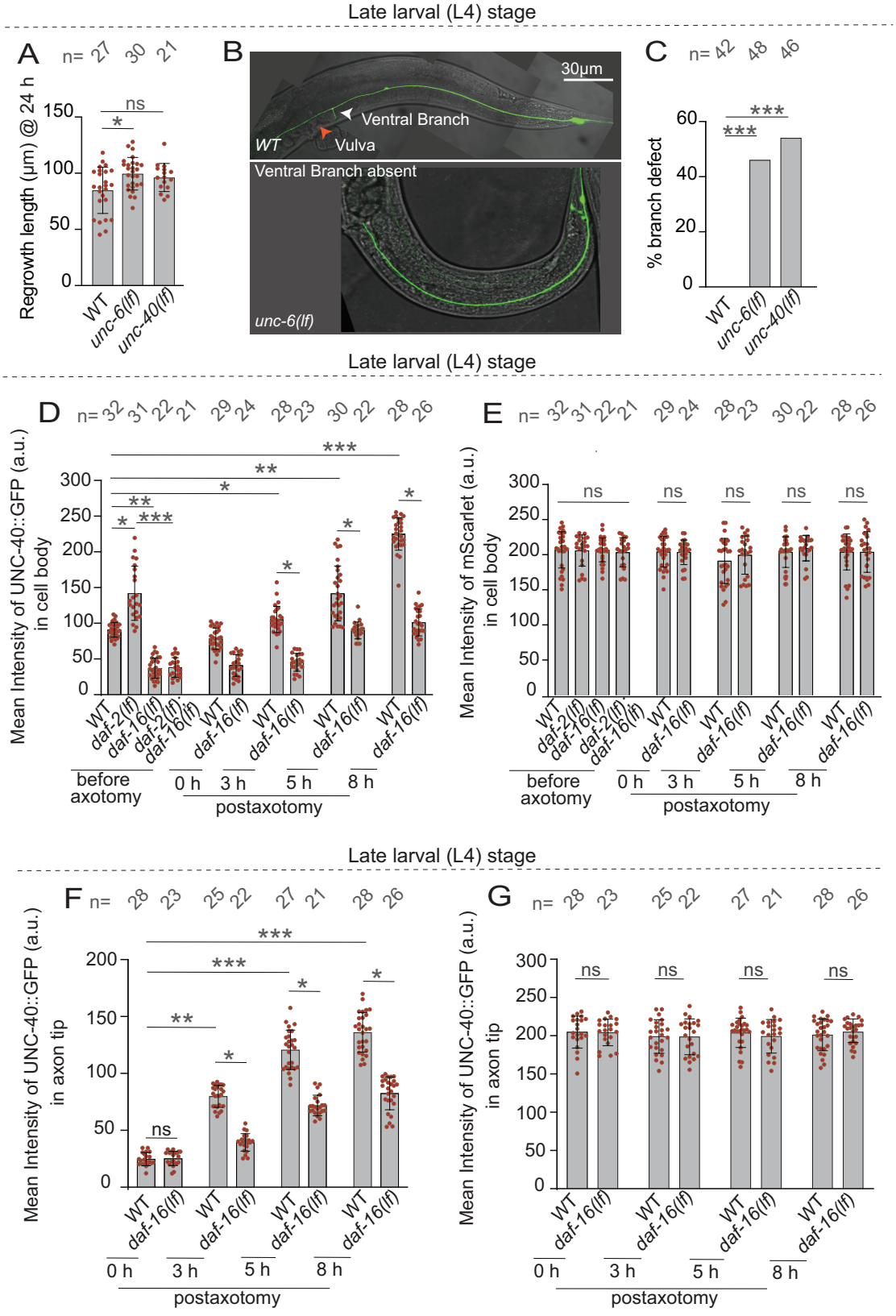

Figure S5: Regulation of the expression and localization of UNC-40 by DAF-16 during axon regeneration, related to Figure 5.

A) The quantification of axon regrowth length corresponding to the 'non-fusion' events in *unc-6(lf)* and *unc-40(lf*) at 24 h postaxotomy at L4 stage. N= 3-4. B) The confocal plus DIC images of PLM neuron expressing P*mec-7*::GFP (*muIs32*) in WT and *unc-6(lf)*. C) The percentage ventral branch defect in *unc-6(lf)* and *unc-40(lf*). N (independent replicates) = 3-5. D-E) The plots represent the mean intensity of *Punc-4*0::UNC-40::GFP [*icIs132*] (D) and P*mec-4*::mScarlet [*shrEx209*] (E) measured from the ROI on the cell body of PLM (in Fig 5D) before and at different time-points after axotomy in WT and *daf-16(lf)*. For both D and E, N= 3-6. F-G) The plots show the mean intensity of P*unc-4*0::UNC-40::GFP [*icIs132*] (F) and Pm*ec-4*::mScarlet [*shrEx209*] (G) from ROI on PLM axon (Fig 5E) before and at different time-points after axotomy in WT and *daf-16(lf)*. In C, ***P < 0.001, Fisher's exact test. In A, D-G, *P < 0.05; **P < 0.01; ***P < 0.001; ns: non-significant; ANOVA with Tukey's multiple comparisons test. Error bars represent Standard Deviation.

Table S1: List of mutants studied for functional restoration assay (excel file).

Click here to download Table S1

Table S2: *Caenorhabditis elegans* strains used in this study.

Click here to download Table S2

Table S3: Strains carrying newly generated extrachromosomal transgenes.

Strains	Transgene	DNA construct	Genetic Background	Concentration,
NBR568	*shrEx209*	P*mec-4*::mScarlet (PNBRGWY54)	N2	5 ng/µl
NBR925	*shrEx435*	P*mec-4*::*unc-9*::GFP (PNBRGWY561)+P*mec-4*::mScarlet (PNBRGWY54)	N2	PNBRGWY561-10ng/ µl PNBRGWY54-5ng/ µl
NBR594	*shrEx224*	P*mec-4*::*daf-16a* (PNBRGWY107)	*daf-16(mu86)* I; *muIs32* (P*mec-7*::GFP) II	10 ng/µl
NBR730	*shrEx311*	P*myo-3*::*daf-16a* (PNBRGWY108)		10 ng/µl
NBR737	*shrEx315*	P*dpy-7*::*daf-16a* (PNBRGWY109)		10 ng/µl
NBR739	*shrEx317*	P*rgef-1*::*daf-16a* (PNBRGWY110)		10 ng/µl
NBR657	*shrEx227*	P*mec-4*::*daf-16f* (PNBRGWY111)		10 ng/µl
NBR732	*shrEx313*	P*myo-3*::*daf-16f* (PNBRGWY112)		10 ng/µl
NBR738	*shrEx316*	P*dpy-7*::*daf-16f* (PNBRGWY113)		10 ng/µl
NBR740	*shrEx318*	P*rgef-1*::*daf-16f* (PNBRGWY114)		10 ng/µl
NBR735	*shrEx320*	P*mec-4*::*daf-16f* (PNBRGWY111)+ P*myo-3*::*daf-16f* (PNBRGWY112)		10 ng/µl (each)
NBR592	*shrEx436*	P*mec-4*::*daf-16f* (PNBRGWY111)	*muIs32* (P*mec-7*::GFP) II	10 ng/µl
NBR593	*shrEx437*	P*myo-3*::*daf-16f* (PNBRGWY112)		10 ng/µl
NBR777	*shrEx389*	P*mec-4*::*dlk-1* (PNBRGWY13)	*muIs32* (P*mec-7*::GFP)II	0.5 ng/µl
NBR779	*shrEx391*	P*mec-4*::*dlk-1* (PNBRGWY13)	*daf-16(mu86)*I; *muIs32* (P*mec-7*::GFP) II	0.5 ng/µl

Table S4: List of the neuronal target genes of DAF-16 categorized under the Gene Ontology term (GO:0097485) or neuronal projection and guidance (excel file).

Click here to download Table S4